Chapter 7

Discussion

The rich experimental results on I_2 in Kr allow for the first time the derivation of the recombination dynamics of a molecule in the condensed phase without the aid of simulations. It is instructive to compare the results obtained purely from experiment with those from DIM-trajectory simulations. The results obtained for I_2/Kr guide the interpretation of the experiments on ClF and Cl_2 by analogy.

Ultrafast energy transfer to the solvent (chapters 7.3 and 7.4) and a strong coupling of potential energy surfaces (chapter 7.6) are observed both in the large and heavy I_2 and in the small and light ClF molecule. Unlike I_2, the small size of the F fragment gives rise to ultrafast reorientation of the molecular bond in recombination dynamics (chapter 7.5) and allows the F atoms to leave the solvent cage (chapter 7.7). The heavy mass of the I_2 fragments and the well defined scattering conditions keep the wave packet much better localized and oscillations in the pump-probe spectra live much longer.

7.1 I_2 in Kr - model data from systematic experiments

A one dimensional representation for the multidimensional potential of excited state surfaces of I_2/Kr is constructed from the pump-probe spectra. In the subsequent chapters experimental snapshots of a wave packet trajectory immediately display the inelastic and nonlinear interaction of the I fragments with the Kr cage. Different signatures of vibrational relaxation in the pump-probe spectra are investigated, and it is demonstrated that the envelope of pump-probe spectra can be exploited to determine vibrational relaxation rates, even if the oscillations are not resolved. The influences of the width of the wave packet and of the probe window are analyzed.

7.1.1 Vibrational frequencies in the B state

Fig. 7.1 shows the observed first periods T_1 as a function of pump energy. The triangles are read from spectra with fixed $\lambda_{probe} = 480$ nm, and the squares for $\lambda_{probe} = 520$ nm (for the original spectra see Appendix). It is evident, that the periods are similar, but they show systematic deviations of up to 10% for the two probe wavelengths. To obtain the correct round-trip times, it is necessary to tune the probe together with the pump wavelength in such a way that the wave packet is probed at its turning point. This consistent variation of pump and probe wavelength yields the solid circles. A discussion of this procedure is presented in chapter 7.1.2.

For pump wavelengths $\lambda_{pump} > 600$ nm the $X \rightarrow A$ transition dominates the absorption spectra, because the Franck-Condon factors of the $X \rightarrow B$ transition decrease rapidly. Unfortunately, every wavelength λ_{probe} that probes the B state near its minimum expected around 640 nm, also probes the A state population. Therefore T_e of the B state could not be measured. Near the minimum, the potential should be only weakly influenced by the matrix and is well described by a Morse potential. The square of the experimental frequencies $\nu^2(E)$ from Fig. 7.1 is linearly extrapolated to estimate T_e, since the frequency of classical vibrations in a Morse potential at energy E is $\nu(E) = \omega_e\sqrt{1 + E/D_e}$. The matrix shifts of ω_e and T_e should be on the order 1 to 2% for valence states (cf. chapter 2.2.3)

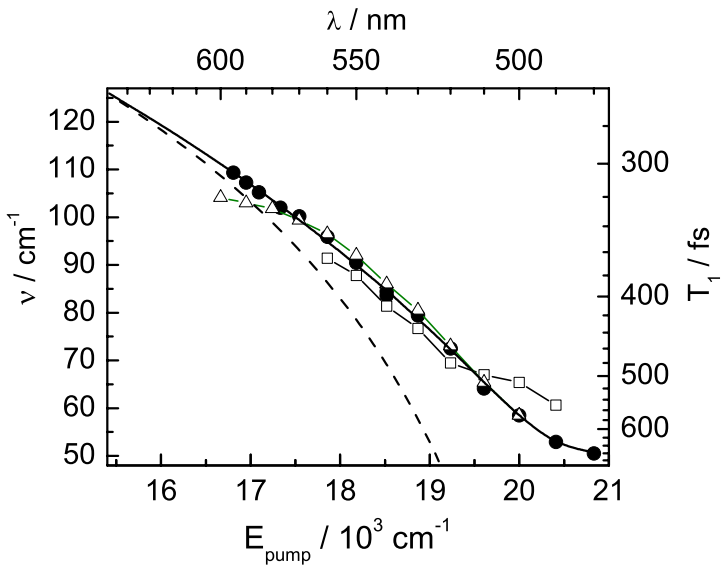

Figure 7.1: First round-trip times T_1 and frequency ν as a function of energy E_{pump}. The solid circles are the correct values determined by probing the wave packet at the turning point via an adjustment of the probe wavelength (see text). Deviations occur if the probe wavelength is kept fixed at 520 nm (squares) or 480 nm (triangles). The dashed line displays the gas phase frequencies corrected for the vertical solvation shift.

and under these constraints the extrapolation yields $\omega_e = 125.9$ cm^{-1} and $T_e = 15420$ cm^{-1} (Tab. 7.1). The function $\nu_f^2(E) = \omega_e(1 + E/D_e) + \exp(-\alpha(E - E_0))$ is fitted to the solid circles, yielding the solid line in Fig. 7.1. $\nu_f^2(E)$ consists of the linear Morse-term and an empirical exponential term, that is negligible below 19500 cm^{-1}. This exponential term describes the deviation of $\nu^2(E)$ from the Morse value at high energies E quite well.

In Fig. 7.1 the $\nu(E)$ curve in Kr is compared to the gas phase (dashed), shifted in T_e by the 350 cm^{-1} due to solvation. The anharmonicity in the matrix is systematically smaller. The repulsive interaction with the cage atoms increases with the elongation R, i.e. with energy E. This bends up the outer wing of the potential in Fig. 7.2. The potential in the matrix for high energies E is closer to the harmonic oscillator, which is expressed in a smaller slope of $\nu(E)$. A Morse-like approximation works well only deep in the well, where the interaction is still relatively weak. Near the dissociation limit the cage walls confine the I fragments and a curvature of $\nu(E)$ with the opposite sign is observed.

7.1.2 Construction of B state potential from pump-probe spectra

The scheme in Fig. 7.2 shows the $X \rightarrow B$ transition induced by the pump beam and the $B \rightarrow E$ transition due to the probe beam. Different X, B and E state surfaces of I_2 in the Kr matrix are derived and explained in the following.

An effective 1-D potential energy surface is constructed from the experimental values (solid circles) for the periods T_1 given in Fig. 7.1. For resolved quantized vibrational levels one would use the RKR (Rydberg-Klein-Rees) [207–209] scheme for the construction of the potential, and here the classical continuum analogue [210] can be applied. If the round-trip times $T(E)$ in a potential $V(r)$ are known for all energies E, the potential can be constructed as follows. The velocity of the classical particle is $v = \sqrt{2(E - V(r))/m}$. Thus an infinitesimal time step is $dt = dr\sqrt{2(E - V(r))/m}$. The potential is constructed successively by going from the potential minimum to higher energies using

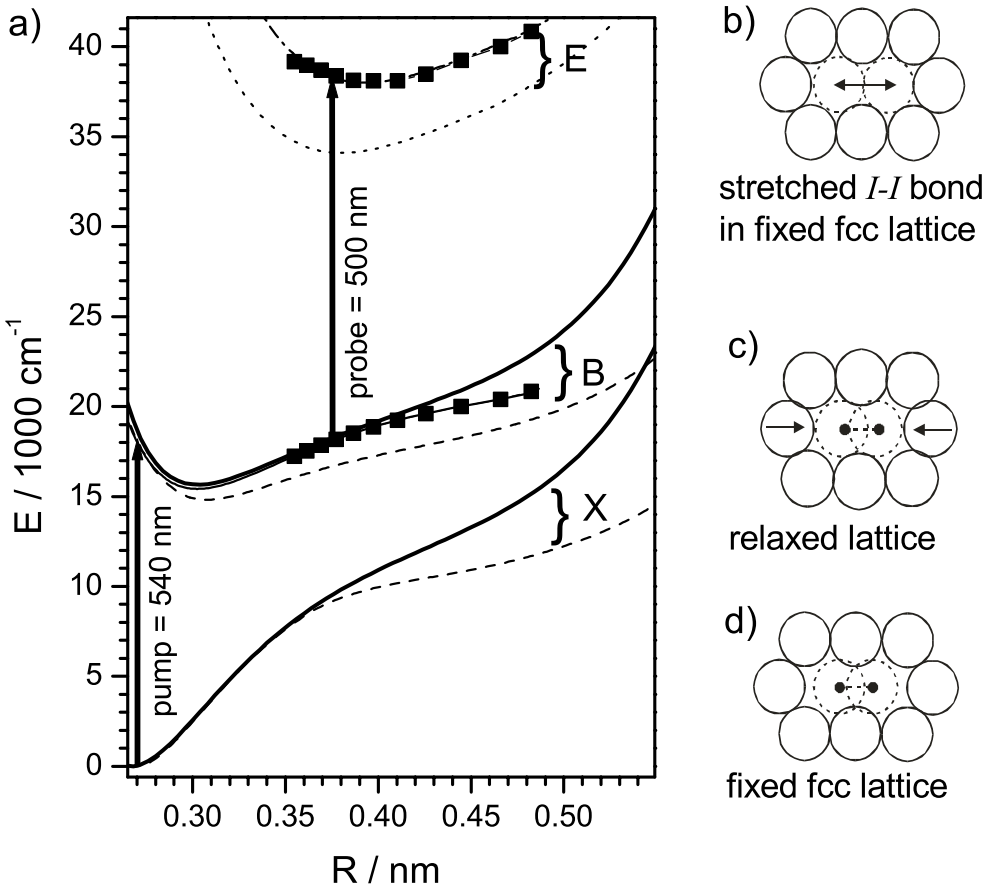

Figure 7.2: a) Potential energy diagram of I_2 in Kr including the ground state X, the valence B state and the ionic E state relevant for the pump-probe spectra. The arrows depict pump and probe transitions. The squares indicate the shape of the potentials as derived from the experiment. Dashed lines correspond to DIM calculations in the fixed Kr fcc lattice (see text and panels b and d) and solid lines to a relaxed cage geometry (see panel c). The dotted line reproduces the E state from ref. [204] for a fixed fcc lattice (see panel b) and the dash-dotted line includes a shift by 0.01 nm outwards and 3900 cm^{-1} up in energy. Panel d) shows I_2 in the ground state surrounded by a fixed fcc lattice. Note the space between I and Kr along the internuclear axis is responsible for the soft potential in this geometry. In panel c) the Kr atoms have relaxed around the molecule, bending the outer limb of the potential up. Fig. 1b shows the I_2 at a bond distance $R = 0.4$ nm typical for a probe transition. Here the fixed fcc lattice approximates a geometry relaxed around the extended $I - I$ bond.

State			I_2/Kr RKR	I_2/Kr DIM	I_2/Kr DIM
		I_2 gas phase[a]	dynamic lattice	relaxed lattice	fixed fcc lattice
		experiment	experiment	theory	theory
B	ω_e / cm^{-1}	125.69	125.9	125.9	116.5
	$\omega_e x_e$ / cm^{-1}	0.764	0.702	0.721	0.783
	T_e / cm^{-1}	15769	15420	15644	14816
E	T_e / cm^{-1}	41411	38000	-	34101[b]

[a] ref. [206], [b] ref. [204]

Table 7.1: Spectroscopic parameters T_e, ω_e and $\omega_e x_e$ for the gas phase, and for I_2 in Kr matrix. Note the RKR method measures a dynamic potential including the lattice response and the DIM calculation is for the relaxed lattice and the fixed fcc lattice, respectively. The parameters for the B-state DIM potential in the relaxed cage agree well with those for the RKR potential within the accuracy of a Morse-fit to the potential. The parameters describe the potential near the minimum and the dynamic potential deviates from the DIM-potential in the relaxed cage only at high energies (cf. Fig. 7.2).

the fitting function $\nu_f^2(E)$. Note that for the construction of the potential by the RKR method, rotational information is needed to find the absolute positions of the inner and outer turning points. In the matrix I_2 does not rotate. Instead, the gas phase Morse potential is kept as the repulsive inner wing of the B-state, since the matrix interaction near the inner turning point is expected to be minimal. Alternatively, one could adopt the inner wing of the calculated DIM potentials. This would shift the outer wing by less the 0.003 nm to larger elongations, which is negligible with respect to the quality of the potential. In essence, the outer wing was determined from $\nu(E)$ by numerical integration and the result is presented in Fig. 7.2 as a solid line with solid squares indicating where experimental points have been measured.

The effective potential incorporates some of the coupling to other modes of the multidimensional system. If classical trajectories are run on this potential, they reproduce the classical frequencies ν_{osc} collected in Fig. 7.1. The frequencies $\nu(E)$ and the derived RKR potential are obtained from the round-trip time T_1 immediately after excitation. The periods are measured for relaxing wave packets. Thus the potential is based on the initial condition of a wave packet prepared on the B-state with the surrounding Kr atoms thermally equilibrated at $T = 15$ K around an I_2 molecule in its ground state – which is the typical situation in pump-probe spectroscopy. However, it should be a good approximation in different situations, as long as the solvent atoms are not too far from this thermal equilibrium. Such a potential is very helpful for quick and precise estimates of the dynamics and to develop an intuitive picture of the multidimensional problem. It also helps to design pump-probe experiments, because the potentials can be directly used to estimate the needed wavelengths and time-resolution.

To give an intuition of the one-dimensional representation of the multidimensional potential and to have a first comparison with experiment, the DIM potential surface for I_2 in Kr was calculated following refs. [63, 64] and including their correct diagonalization of the Hamiltonian matrix. The results are shown in Fig. 7.2a. The dashed lines correspond to calculations of the X and B states where the Kr atoms are kept fixed at the fcc lattice positions (Fig. 7.2d). This is the geometry for which potentials are shown in refs. [63, 64]. For the solid lines, the Kr atoms are relaxed around an I_2 molecule in the X state. In this geometry the two Kr atoms, that are in line with the I_2 axis, move closer to the I atoms (Fig. 7.2c). Stretching the molecular bond of I_2 against this solvent cage, with the Kr atoms fixed at this position, induces a steeper outer limb in the potential. Comparison of the DIM potentials with the experimental RKR potential shows that – not surprisingly – the relaxed cage geometry gives a better agreement. However, close to the dissociation limit the RKR potential

is softer, since it includes the cage dynamics. In the course of the $I-I$ stretching motion, the Kr atoms are pushed out, which bends the outer limb of the potential towards the loose fcc cage. This phenomenon is expected to be accurately reproduced by the averaged DIM trajectory calculations, discussed below in chapter 7.3.1. Note that the repulsive interaction between I and Kr shifts the potential minimum of the B state up by 600 cm^{-1} upon cage relaxation (cf. also Fig. 2.6).

The spectroscopic constants that reflect the situation near the minimum are collected in Tab. 7.1. The calculations for a fixed fcc lattice (dashed lines in Fig. 2.6) yields significantly lower T_e and ω_e and an anharmonicity $\omega_e x_e$ closer to the gas-phase value. To get the correct values, the calculations have do be performed in a relaxed geometry (solid lines). These values agree well with the gas phase and the RKR result. At higher excitation, the anharmonicities change and the potentials differ for large R (cf. Fig. 7.2). These deviations would be described by higher orders of the anharmonicity. The DIM potentials in the fcc or relaxed configuration of the cage are calculated for fixed Kr atoms. The RKR potential includes the cage dynamics, which bends the potential down at large R. The shape of the potential near the minimum is only weakly affected and Tab. 7.1 only compares the "constants" near the minimum. In chapter 7.3.1 , the calculation of a "trajectory averaged" potential will be proposed which will approximate the measured potential at large R, as well.

A similar analysis for ClF/Ar in the excitation region relevant for this thesis cannot be accomplished. It will be interesting to apply the method again in the bound region of the B state of ClF. These experiments are expected to be rather difficult due to the small Franck-Condon factors in this region; However, it will be interesting to compare the dynamics of the light ClF molecule in the bound region to the very detailed corresponding dynamics of I_2.

7.1.3 Construction of E state from pump-probe spectra

The vibrational frequency $\nu(E)$ of the B state was derived in section 7.1.2, without assumptions concerning the shape of the E state or the difference potential ΔV. Having constructed the B state potential $E_B(R)$ in the previous section by tuning the pump wavelength and optimizing the probe wavelength, the dependence of the pump-probe spectra on the probe wavelength can now be exploited in addition to construct the final E state energy surface $E_E(R)$.

To that end the optimal probe photon energy $h\nu_{probe}$ is identified, which records the wave packet just at the outer turning point R_{win}. For $\lambda_{pump} = 540$ nm the corresponding probe wavelength is 520 nm (cf. Fig. 6.3). The first criterion for probing at the turning point is the observation that the double splitting of the oscillation due to inward and outward motion just disappears. The second criterion is vanishing $\tau_m \approx 0$, i.e. the shortest probe wavelength is chosen, for which the maximum of the envelope is close to time $t = 0$ (cf. Fig. 6.7). $h\nu_{probe}$ determined in this way corresponds to the difference potential, $h\nu_{probe} = \Delta V = E_E(R_{pump}) - E_B(R_{pump})$, at the turning point R_{pump} in the Franck approximation [104]. Since the B state potential, $E_B(R)$, is known from the preceding chapter, the final state $E_E(R)$ can be obtained by adding $h\nu_{probe}$ to the B state energy in Fig. 7.2 at the position $R = R_{win} = R_{pump}$. The experimentally determined points (squares) are compared to the surfaces given by Batista and Coker (dotted) [204]. Concerning the shape $E_E(R)$ of the ionic E state surface, the results obtained by Batista and Coker [204] in the fixed fcc cage (Fig. 7.2b) agree very well with the experimentally determined potential (squares), if the potential is shifted by 0.01 nm outward and 3900 cm^{-1} up in energy (dash-dotted line). Here the experiment probes the potential at $I-I$ elongations around 0.4 nm, which is the nearest neighbor distance in Kr (Fig. 7.2b). This renders the fixed fcc lattice, used in the calculations, a good approximation.

The minimum $T_e(E)$ of the ionic E state derived experimentally is compared to the gas phase and the result by Batista and Coker in Tab. 7.1. The large red shift of 3400 cm^{-1} with respect to the gas phase, derived experimentally, is typical for the solvation of ionic states (chapter 2.2.3). The calculation by Batista and Coker yields a red shift of 7300 cm^{-1}, which is more than twice as large.

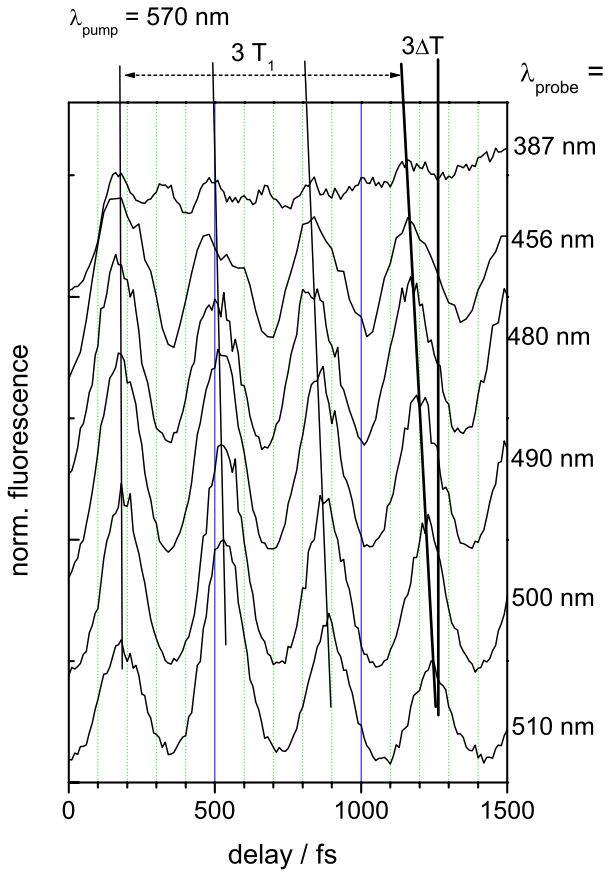

Figure 7.3: Pump-probe spectra with pump wavelength fixed at $\lambda_{pump} = 570$ nm to demonstrate the effect of the probe window. The lines indicate the decrease ΔT of the measured period T_1 with decreasing probe wavelength. After 3 periods the difference for $\lambda_{probe} = 510$ and 456 nm has accumulated to $3T_1 = 70$ fs.

This may originate from the fixed fcc Kr structure used in the calculation or from the empirical shifts introduced in the DIIS formalism.

7.2 Window effects in condensed-phase pump-probe spectra

At first glance, one would assume that it is only the pump pulse which determines the frequency of the oscillations observed in a pump-probe experiment, as it prepares certain vibrational levels. In this case, the differences Δt_1 or Δt_2 between the parallel lines, e.g. in Fig. 6.3, for inward or outward motion correspond to the correct round-trip time T_1. However, this is not the case, and a systematic deviation of T_1 or ν values is obtained in Fig. 7.1, if, for example, probe wavelengths of 480 nm (triangles) or 520 nm (squares) are used.

For a demonstration of this effect consider Fig. 7.3, which displays spectra with a fixed pump wavelength of 570 nm. With $\lambda_{probe} = 480$ nm the wave packet will be recorded just at the turning point (cf. Fig. 7.2). $\lambda_{probe} = 456$ nm already results in a considerable broadening of the peaks.

In order to form a wave packet, it is necessary to coherently excite a superposition of several vibrational levels according to the spectral width of the pump pulse wave packet $\Delta\nu$. Fig. 7.4 schematically shows the projection of the ground state population onto the B state, with a pump pulse of frequency ν_{pump} and bandwidth $\Delta\nu_{pump.}$ The bandwidth determines which part of the Gaussian wave function in the ground state is promoted to the excited state, leaving a hole in the ground state wave function after excitation. On the B state, this gives amplitude to the vibrational levels which lie within the bandwidth. A contour plot of the wave packet moving outwards is indicated. The difference potential ΔV to the E state at R_{win} likewise determines how the spectral bandwidth $\Delta\nu_{probe}$ is transformed to the spacial width of the probe window ΔR_{win}. This in turn defines which vibrational levels are

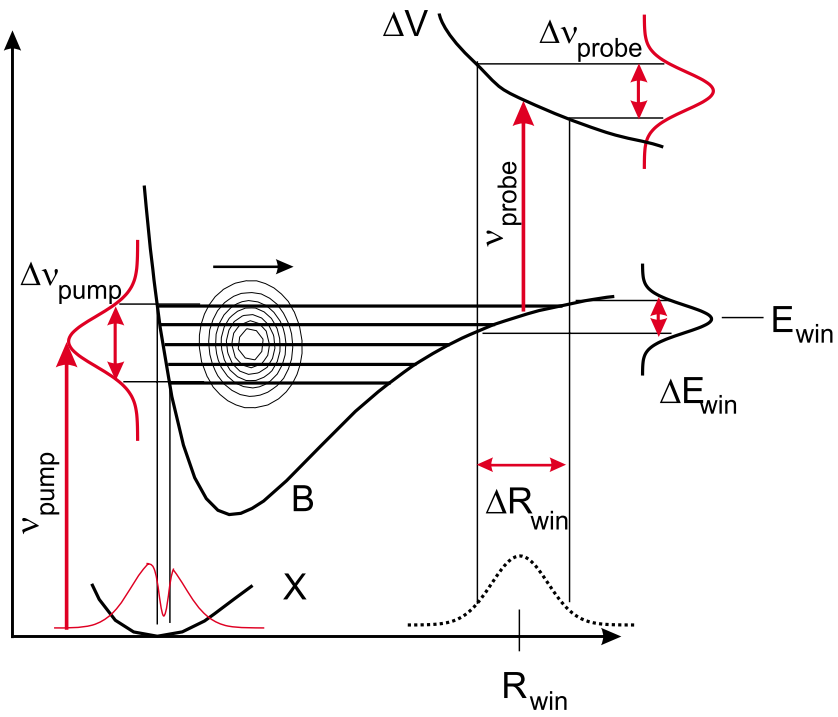

Figure 7.4: Potential diagram showing the ground state X, the excited state B, and the difference potential ΔV to the final state E. The spectral shape of the pump pulse with mean frequency ν_{pump} and bandwidth $\Delta\nu_{pump}$ determines, which vibrational states of the B state are populated. The projection onto the repulsive limb of the B state yields the hole burned into the ground state population. Likewise, the projection of the probe pulse onto the difference potential ΔV yields the probe window R_{win}. The outer limb of the B state then determines which vibrational levels are probed, i.e. the energy of the probe window E_{win} and the probed bandwidth ΔE_{win}.

probed within ΔE_{win}. In the example shown in Fig. 7.4, only the upper two of the excited vibrational levels are probed. The anharmonicity yields a longer apparent vibrational period T_1 compared to the center of the wave packet.

If the probe wavelength λ_{probe} is reduced, the probe window moves spatially inward and to a lower energy E_{win}. Thus the less energetic parts of the wave packet, which have a shorter period according to the anharmonicity, gain in weight and the measured period T_1 is reduced. This effect can be clearly seen in the experimental spectra shown in Fig. 7.3. Although the spatial shift is not large enough to yield a resolved splitting, the differences between the maxima indicate a smaller T_1. In essence, the part of the wave packet at E_{win} gains the highest detection efficiency (chapter 2.3.1). This is the wave packet for which the probe window is at the turning point.

Since the effect accumulates, three periods are displayed in Fig. 7.3 to make it clearly visible. The time difference $3T_1$ for $\lambda_{probe} = 456$ nm corresponds to 990 fs and to 1060 fs for $\lambda_{probe} = 510$ nm. This results in a variation of T_1 from 353 fs for probing above the turning point with 510 nm to 330 fs for probing too deep with 456 nm. This error of $\Delta T_1/T_1 = 0.07$ fully explains the systematic difference between the results with probe wavelength fixed at $\lambda_{probe} = 480$ or 520 nm in Fig. 7.1. A correct determination of T_1 requires a tuning of λ_{probe} just to the turning point for each λ_{pump}. The error in the round-trip times T_1 on the order of 7 % is serious, because the anharmonicity is the derivative $d\nu/dE$ of the $\nu(E)$ curve in Fig. 7.1. The slope of $\nu(E)$ differs by more than 50% for the

solid circles and the triangles at low energies. The correct T_1 values given by the circles in Fig. 7.1 were derived by an optimization of λ_{probe} for each value of E_{pump}.

It is instructive to complement this explanation with arguments from the classical MD simulations [26]. If the trajectory travels high above the window, it moves with more kinetic energy and larger velocity through the window. It spends less time in the window, diminishing the detection efficiency. Thus the low energy trajectories with too short periods T_1 dominate the experimental spectrum. If the average energy of the trajectories lies below the window, only the fraction with high energy reaches the probe window, and the apparent T_1 is too long. These classical arguments are in full accord with a quantum mechanical Franck-Condon picture.

Changes of the observed oscillational period with probe wavelength have already been observed in trajectory simulations [27]. There they have been used to estimate the probe window position, since it could not be deduced from the systematic variation of the probe wavelength in the experiments. The position of the probe window has a dramatic influence on the decay of the envelope of the pump-probe spectra in these simulations [27] and thus also on the predissociation time deduced from the simulations. The experimental approach just discussed has the advantage to separate the processes of vibrational energy relaxation and predissociation. This was applied recently to determine predissociation rates and to clarify the interplay of vibrational relaxation and predissociation rates [115, 116]. Thus, tuning both pump and probe wavelength proves to be helpful even when a high level simulation is at hand, i.e. to judge, if systematic errors are introduced by the simulation of the probe process.

In the gas phase, where oscillations in the B state of I_2 can be observed for hundreds of ps, the Fourier transformation yields clearly resolved vibrational levels that are pumped and probed. The spectrum of the probe pulse then changes the intensity of the individual vibrational lines in the observed Fourier transform.

7.3 Wave packet dynamics with strong fragment-cage interaction

7.3.1 Construction of an $I - I$ trajectory from pump-probe spectra

The spectra in Fig. 6.2a show that the time spent between the first outward ($\rightarrow$) and inward passage ($\leftarrow$) for the fixed probe window ($\lambda_{probe} = 500$ nm, $R_{win} = 0.376$ nm) increases dramatically from 120 fs, for $\lambda_{pump} = 540$ nm, up to 350 fs for $\lambda_{pump} = 490$ nm, whereas that for the second outward/inward passage stays essentially constant at 120 fs. The energy corresponding to $\lambda_{pump} = 500$ nm is close to the gas phase dissociation limit. Obviously, the interaction of an essentially free I atom ($\lambda_{pump} = 490$ nm) with the cage atoms around the outer turning point takes a much longer time than for a bound one ($\lambda_{pump} = 540$ nm). The collision of the free I atom with the Kr cage is connected with such a high energy loss that the bond cannot be stretched as far in the second round-trip. Snapshots of this interaction are recorded now in Fig. 6.2b) by scanning the probe wavelength from $\lambda_{probe} = 540$ nm to 480 nm and therefore the probe position R_{win} from 0.36 nm to 0.45 nm for an excitation at the dissociation limit ($\lambda_{pump} = 500$ nm). The probe window positions R_{win} for the respective wavelengths are plotted as a function of time (open circles in Fig. 7.5a, given by the maxima in the pump-probe spectra of Fig. 6.2b). The positions are connected by a smoothed line to yield the time course $R(t)$ of a mean trajectory (solid line in Fig. 7.5a) for the first three excursions I to III. The circles for the inner turning point near 0.27 nm are estimated from the potential together with the energy loss derived in Fig. 7.11. The wave packet reaches out to 0.43 nm only in the first excursion, and already in the second one it does not go beyond 0.39 nm. The most interesting first excursion is asymmetric. The outward motion is still rather sinusoidal, and from the window at 0.36 nm to the turning point it takes about 100 fs. The return is extremely delayed, and especially around 300 fs the wave packet is not accelerated on the way back to the potential minimum as expected, but it is further slowed down. The return from the turning point to the 0.36 nm window takes more than 250 fs.

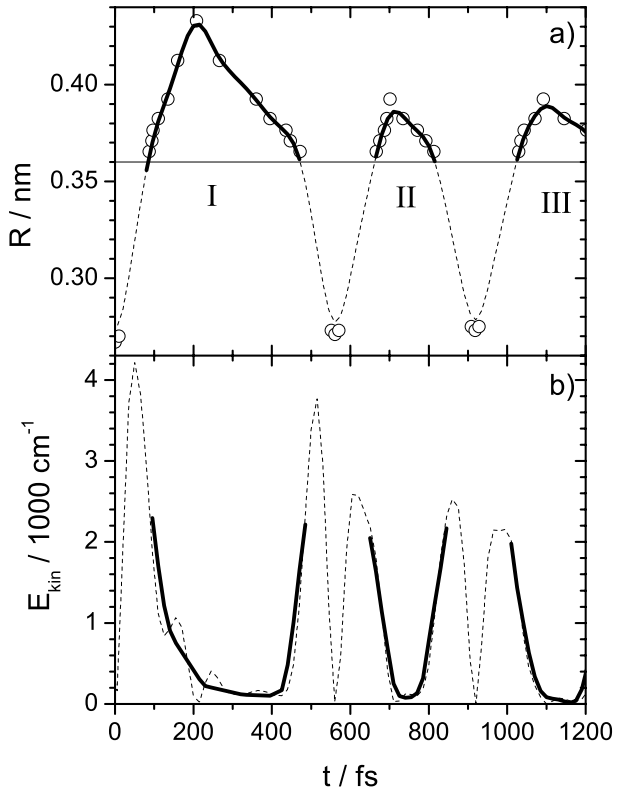

Figure 7.5: a) Trajectory $R(t)$ (solid line) showing $I - I$ separation R versus time t as derived from the maxima in the pump probe spectra for $\lambda_{pump} = 500$ nm. (Fig. 6.2b). Only the outer bow between 0.36 nm and 0.43 nm is covered by probe windows and I - III indicate the first three excursions. The kinetic energy $E_{kin}(t)$ is obtained from differentiation (weak dashed line) and smoothing (thick dashed line)

Differentiation of $R(t)$ versus time yields the local velocity $v(t)$, presented as kinetic energy $E_{kin}(t) = \frac{1}{2}\mu v^2(t)$ as the dashed line in Fig. 7.5b), where μ is the reduced mass of I_2. The mild undulations may be artifacts due to the differentiation and the kinetic energy only relies on the measured data points in the region of the thick smoothed line. Around the inner turning points, it depends on the interpolation and should be close to a free oscillator. The maximal kinetic energy is consistent with the excitation 4230 cm^{-1} above the minimum of the B state. The snapshots of the oscillation were taken on the relevant outer limb of the potential and the corresponding kinetic energy $E_{kin}(t)$ is emphasized by the thick solid line. It shows a deceleration on the way to the outer turning point as expected for a Morse potential, but the acceleration on the way back is completely different. The trajectory moves extremely slowly for a long time, between 200 and 400 fs with only $E_{kin} \approx 200$ cm^{-1}. On a Morse potential it should have already 2000 cm^{-1} at 300 fs. It seems as if the I atoms stick to the cage wall and move back very slowly together with the cage. This peculiar behavior is demonstrated in Fig. 7.6a on the outer limb of the potential surface of the B state. The energy loss derived from the trajectory is supported by the analysis of the vibrational relaxation rates in chapter 7.4.2. A wave packet excited with $\lambda_{pump} = 520$ nm travels out and returns with an energy loss of 455 cm^{-1}. A wave packet pumped with 500 nm lies significantly higher in energy and reaches much farther out on the soft wing of the potential, then it sticks to the potential energy surface and does not gain kinetic energy. It slides down along the potential surface far below the energy of the 520 nm wave packet until it finally gains kinetic energy.

Comparison to classical trajectory calculations

The dynamics at the dissociation limit (Fig. 7.5) determined for $\lambda_{pump} = 500$ nm can be qualitatively compared to the classical calculation ($\lambda_{pump} = 510$ nm) in ref. [27]. The simulations create a swarm of trajectories. Unfortunately only an "anecdotal" trajectory is presented [27] instead of an

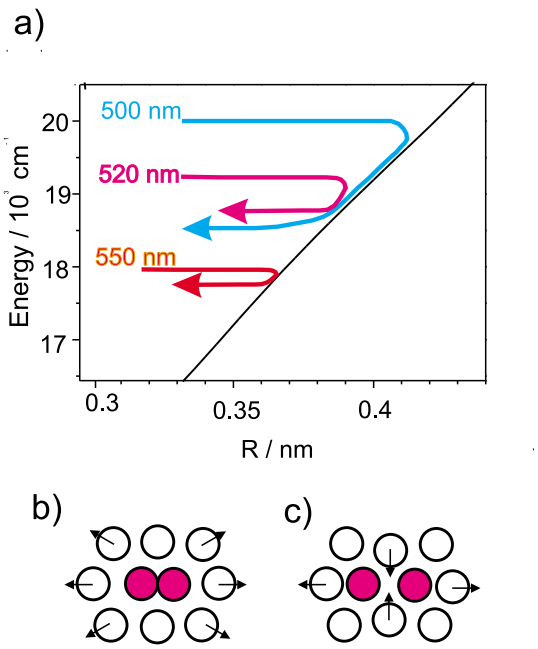

Figure 7.6: a) Sketch of potential and kinetic energy showing the peculiar dynamics of the I_2 molecule for strong fragment cage interaction. In the first collision a wave packet started near the dissociation limit ($\lambda_{pump} = 500$ nm) is scattered below a wave packet that was started at lower energy (i.e. $\lambda_{pump} = 520$ nm). During the interaction the kinetic energy is very small (Fig. 7.5). The energy after the collision is given by the energy relaxation rate (Fig. 7.11). b) Two cage modes according to [37] illustrate the intuitive breathing of the cage and the belt mode that slows down the I fragments in the recombination event (see text).

averaged trajectory with a distribution. In any case, the simulations catch the very strong fragment-cage interaction that allows only one large excursion beyond $R = 0.4$ nm. Similar to the averaged potential discussed above, a comparison of an averaged trajectory with the present experimentally derived trajectory could improve the value of the comparisons and would yield a deeper analysis.

The explanation for the apparent sticking of the I atom to the cage is most evident from a simulation of Cl_2 in Ar near the dissociation limit [37]. Recall from chapter 2.2.1 that Cl_2 in Ar is isolated on double substitutional sites, just like I_2 in Kr. Three modes of deformation are excited with large amplitudes. An expansion of the cage along the $Cl - Cl$ axis excites two modes. The cage breathing, displayed in Fig. 7.6b), is intuitively expected. The second mode (c) contracts a belt of 4 matrix atoms, which lie in a plane perpendicular to and in the center of the $Cl - Cl$ bond. The expansion of the $Cl - Cl$ bond displaces matrix atoms along the bond direction and creates space just around the center of the bond. The atoms in the belt can move inwards and thus compensate the volume change from the $Cl - Cl$ expansion. This picture is valid also for the I_2 in Kr case [29] in accord with the discussion in ref. [37] and with essential features of the simulations on the A state of I_2 in Ar matrix [21]. Now, when the I atoms are stopped at the turning point and try to return, they first have to displace the matrix atoms in the tightened belt, which delays a recombination. The acceleration of these belt atoms takes out kinetic energy from the $I - I$ coordinate. This reduces the I velocity as seen in the sliding down on the potential surface in Fig 7.6a and explains the extremely large energy loss. The usual Morse-like rise in kinetic energy appears only after the belt atoms have been expelled around 400 fs in Fig. 7.5. The experimental trajectory in Fig. 7.5 directly displays this peculiar process.

Comparison to DIM-trajectory calculations

In trajectory calculations using DIM potentials (diatomics in molecules) [108], the potential felt by the I_2 including all Kr atoms is derived (eigenvalues of the Hamiltonian) at each time step for each trajectory.

Fig. 7.7a shows the potential surfaces for the system I_2/Ar as a function of time, as they are usually plotted in publications that report DIM trajectory calculations by Batista and Coker [64]. The data were kindly provided by N. Yu from the group of Coker. Only a selection of 7 states from the 36 valence states is shown. Unfortunately, similar trajectories for Kr are missing and also data for

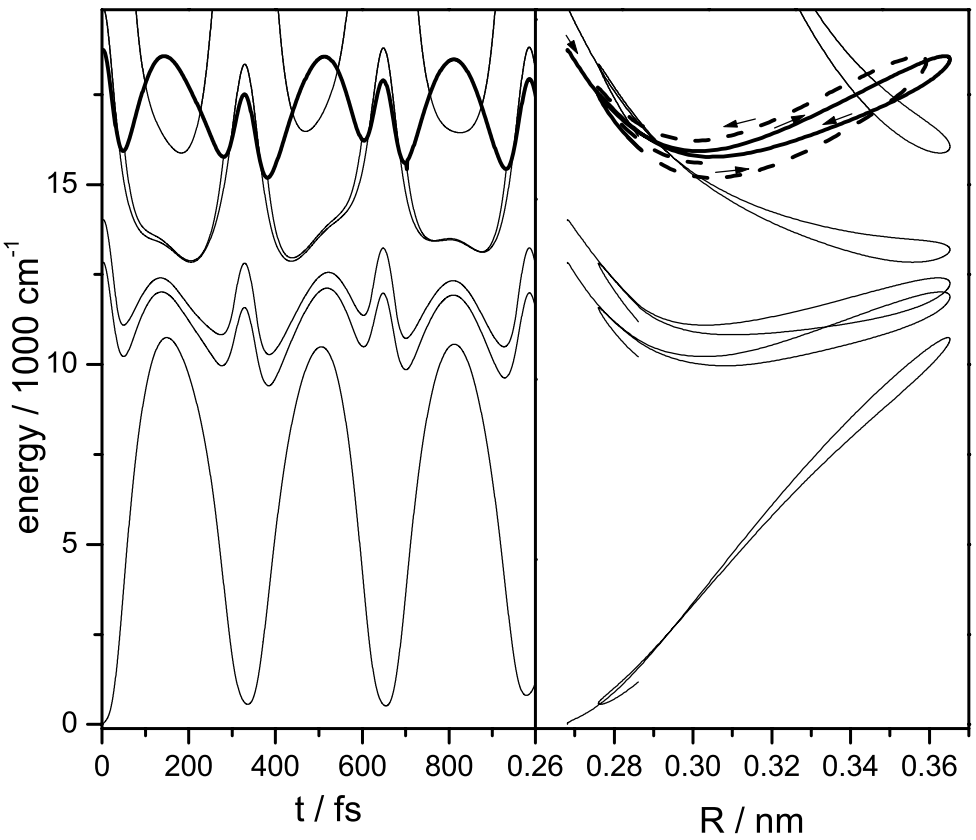

Figure 7.7: a) Potential surfaces of I_2/Ar valence states from a DIM-trajectory as a function of time (data provided by Ning Yu from the group of Coker). The thick line indicates the B state, which is occupied in this trajectory. b) Same trajectory for the first round-trip (up to 350 fs) as a function of R. The potential is higher for the outward motion, than for the return, since the Kr atoms are pushed to the side. The thick solid line indicates the first and the thick dashed line the second round-trip in the B state.

the ionic states are not available. In Fig. 7.7b the same surfaces are plotted as a function of the bond distance R for the first round-trip ($t = 0$ to 360 fs). For the B state, which is populated in this trajectory, two periods (till $t = 700$ fs) are plotted. The first round-trip is depicted by the thick solid line and the second round-trip by the dashed line. Some qualitative results can already be picked out from this simple approach. The trajectory starts at $R = 0,266$ nm and moves outwards, collides with the Ar atoms, loses energy and travels back at a lower energy. For this reason the inner turning point now is at $R = 0,275$ nm. The trajectory moves back out at even lower energy and at the outer turning point a collision with a hot Ar atom transfers energy back into the $I - I$ coordinate.

The plot represents the collision events of a single trajectory. The pump pulse in the experiment prepares a coherent wave packet with a quantum mechanical uncertainty in phase space. Therefore, an ensemble average over many trajectories is required. The mean value of the potential for these trajectories corresponds to an average 1-D potential seen by a wave packet "on the fly" and it should be compared to the surface (Fig. 7.2a) constructed from the experiment. However, such "trajectory averaged" potentials are not available, even though it is a much better approximation than any potential calculated for a fixed lattice. The outward and inward motions are not symmetrical due to the energy loss from the $I - I$ coordinate. In the DIM trajectory calculation, one could even get rid of this problem by constructing two potentials - one for outward and one for inward motion.

Up to now, only simulated signals for special pump-probe combinations have been compared to experiment, and sometimes errors in the simulation compensate each other. One example for such an error compensation can be found in the earliest simulations [64]. It explains the entire pump-probe signal with $\lambda_{probe} = 400$ nm by probe transitions from the A state, and very good agreement is obtained. From the experiment it is obvious, however, that the signal originates from probing B and this is proved by the experimental determination of the time zero, which was not known at the time of the simulations. The error has now been corrected [66], resulting now in a much weaker nonadiabatic coupling of the B state to the predissociating states.

The potential constructed entirely from the experiment (Fig. 7.2a) may advance the understanding of the ultrafast manybody dynamics, since a detailed theoretical modeling of the probe process to the ionic surfaces is circumvented and the simulations are compared to the experiment at an earlier stage. It imposes a test onto the simulation in a systematic way. The computation of the ionic surfaces is very tedious work and therefore it is only accomplished rarely in trajectory simulations. In the theoretical support for the ClF experiments this task is still out of reach.

7.3.2 Recombination dynamics of ClF in Ar

The pump-probe spectra for ClF in Ar are not as well modulated as the I_2/Kr spectra. Nevertheless, the oscillations due to wave packet motion can be used to determine the ultrafast dissipative dynamics. The early wave packet motion after excitation with $\lambda_{pump} = 387$ nm above the dissociation limit can best be displayed for a probe window near this limit, i.e. at $\lambda_{probe} = 319$ nm. The recombination dynamics can be seen and the population that relaxes further down in the potential well is not probed and thus does not contribute to an unwanted background signal. The first 3 ps of the spectrum are shown on an enlarged scale in Fig. 7.8b. The following interpretation of the spectrum is analogous to the I_2 system discussed in the preceding chapter.

The first strong maximum after 50 fs catches the wave packet when it moves outwards ($\rightarrow$) through the probe window for the first time. The minimum around 250 fs corresponds to the time when it is beyond the probe window. There it smashes into the cage and loses most of its energy, which forces the wave packet to travel back. Thus the shoulder after 500 fs displays the wave packet, when it passes the probe window for a second time on the inward motion ($\leftarrow$). Next, it reaches the inner turning point and subsequently passes the probe window a third time, about 850 fs after the first peak. Due to the strong collision in the first excursion it has already lost most of its kinetic energy. The

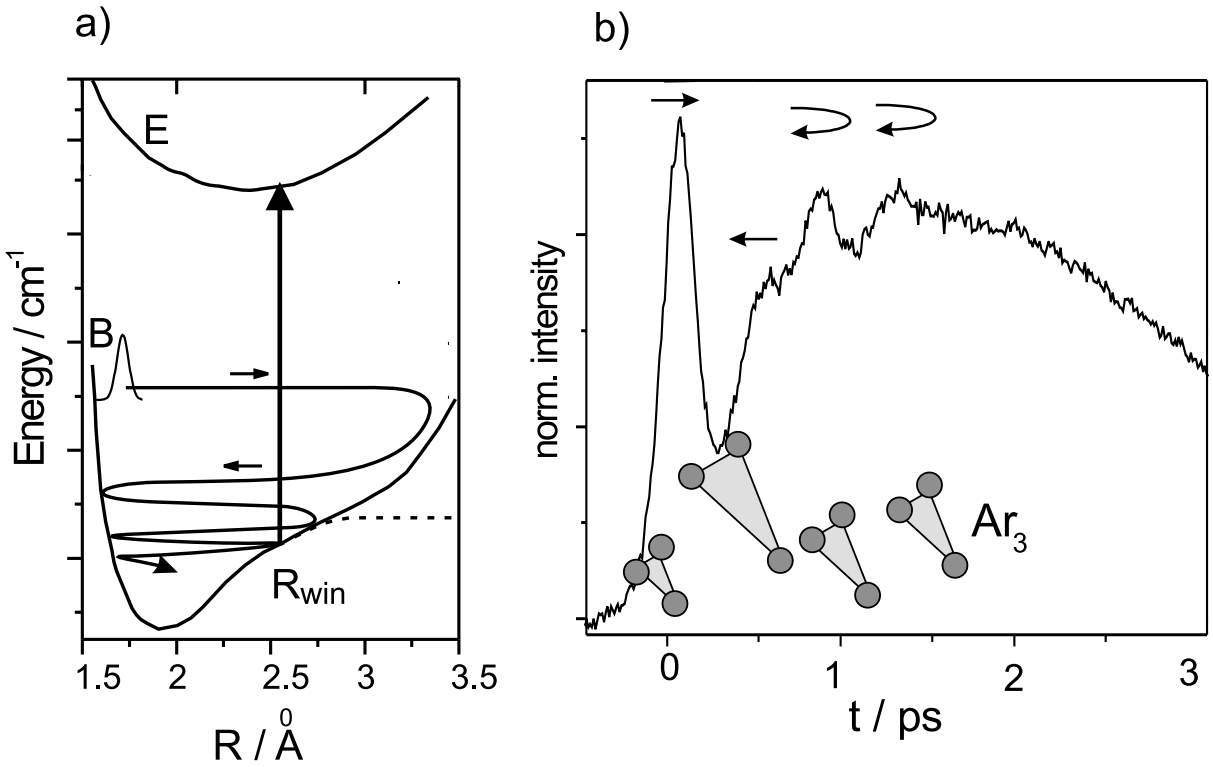

Figure 7.8: a) Scheme of the wave packet dynamics observed in the pump-probe spectrum (panel b) with the probe window at R_{win}. The wave packet is excited (vertical arrow) above the gas phase dissociation limit (dashed) and loses energy in the B state due to interaction with the cage. b) fs-pump-probe spectrum with $\lambda_{pump} = 387$ nm and $\lambda_{probe} = 319$ nm. The arrows above the peaks indicate, how the wave packet passes through the window. The Ar_3 breathing mode is sketched below (see text).

turning point and the probe window in the third passage lie closer together, and the wave packet is only probed once on its outward and inward motion. Finally, after 1250 fs it shows up once more at the turning point. Thus three periods are resolved (cf. Fig. 7.8), and the first one is doubled due to a separated detection of outward and inward motion. The dynamics are sketched in the left panel of Fig. 7.8 in analogy to the trajectory derived for $I_{2,}$ and consistently with the peaks in the fs-pump-probe spectrum and the relaxation time analysis (chapter 7.4.3). The wave packet rides on a background increasing with time, because of dispersion [32], caused by the anharmonicity and because the first strong collision induces decoherence [211]. The latter forces the wave packet dynamics to enter the regime of population relaxation. The main conclusion of the dramatic energy loss in the first collision is substantiated by the analysis of vibrational relaxation in chapter 7.4.3 and supported by DIM-trajectory simulations [71].

From the second to the third period, a round-trip time of about 400 fs is derived, as expected according to the simulation of an F_2 molecule oscillating in the cage structure discussed below. The difference of 350 fs between the shoulder and the second maximum is shorter, because it does not correspond to a full round-trip. The time of 450 fs, spent on the outer bow from the first peak to the shoulder is remarkably long, similar to the corresponding dynamics of I_2/Kr (chapter 7.3.1). These experiments show that the velocities are especially slowed down just after the collision due to the details of the deformation of the cage and the energy losses involved in it. The question deserves some consideration, whether the recombination dynamics of the heavy $I - I$ molecule in the lighter Kr surrounding is comparable to the recombination dynamics of the asymmetric ClF molecule in

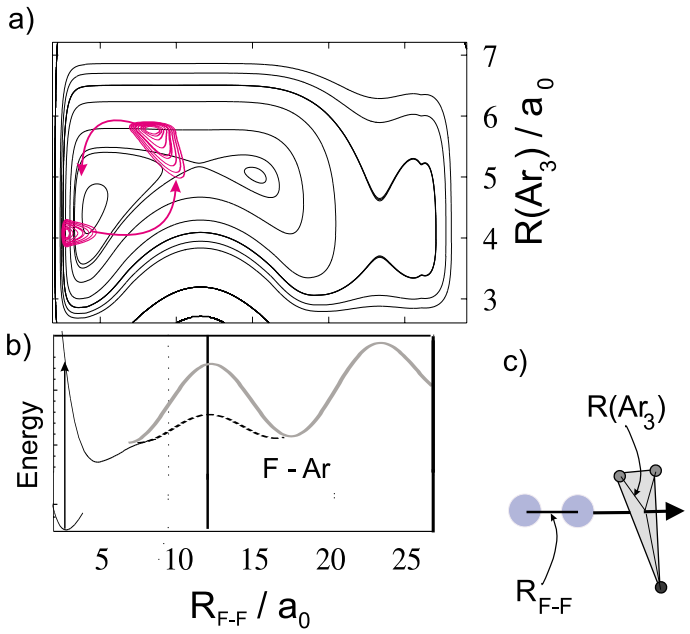

Figure 7.9: a) 2-D potential energy surface of F_2/Ar calculated by G. Chaban [73]. The horizontal axis is the $F-F$ distance and the vertical coordinate is the breathing of the Ar_3 triangle. The geometry is fixed with the $F-F$ coordinate perpendicular to the triangles. b) 1-D representation of the potential surface. The first barrier is greatly suppressed (dashed) when the Ar_3 window is expanded. c) Geometry that defines the F_2 bond distance R_{F-F} and $R(Ar_3)$ as the distance of one Ar to the center of mass of the three Ar.

Ar, where the F fragment has only half of the mass of an Ar atom. The I fragments are heavier than Kr and undergo head-on collisions with one Kr atom and the belt of four Kr atoms moves inward. In contrast, the dissociation of ClF leads to a symmetric collision of the Cl and the F atom each with a triangle of Ar atoms (Fig. 2.5c). A plausible consideration is to take all atoms as hard spheres with van-der-Waals radii, which yields kinetic energy losses of 54 % and 67 % for Cl and F respectively. The deformation will enhance the losses.

A characteristic feature of the spectra in Fig. 7.8b) is the first sharp maximum and a minimum around 250 fs. Both signatures are emphasized near the threshold of $\lambda_{probe} = 320$ nm for the probe resonance and attenuate at shorter probe wavelengths (cf. Fig. 6.9)[1]. The analog phenomenon shows up also in the I_2/Kr spectra (Appendix, e.g. $\lambda_{pump} = 500$, $\lambda_{probe} = 540$ nm) when the probe wavelength is just at the threshold. In the minimum energy configuration of F_2 in Ar at 5 K the molecule is located in a single substitutional site with each F atom pointing at a symmetric triangle of Ar atoms [68] and a similar geometry is likely for ClF (Fig. 2.5c). The collision of the F atom with the triangle leads to cage expansion and breathing. The ionic E state is significantly red shifted in the matrix by solvation of the dipole [205]. The solvation is reduced on expansion of the Ar cage and the E state moves up in energy. The probe wavelength of 319 nm is just at the threshold for reaching the E state (Fig. 7.8a) and the probe window will be lost in the expanded cage. Cage expansion starts with the first collision occurring just after the first maximum in Fig. 7.8b. The sensitivity decreases during the expansion leading to the reduced intensity of the subsequent shoulder. Full sensitivity will be reached again after a period of the Ar breathing mode which appears in Fig. 7.8b around the second maximum and after 800 fs delay. Such a period of the Ar breathing mode is in good accordance with simulations and experiments for doped Ar matrices [212–215].

Support from theory

The interplay of the dissociation of the diatomic with the cage breathing is investigated in a 2-D wave packet simulation on the symmetric F_2 molecule in the fcc argon lattice [72, 73]. One coordinate is the $F-F$ stretch and the other coordinate is the breathing mode of the Ar_3 triangles, at which the F atoms are pointing. All other Ar atoms are frozen and enforce a cage potential. The potential energy surface is shown in Fig. 7.9. The barrier due to the nearest Ar triangle is located at an $F-F$

[1] From 291 nm on the peak increases again due to excitation of Cl_2.

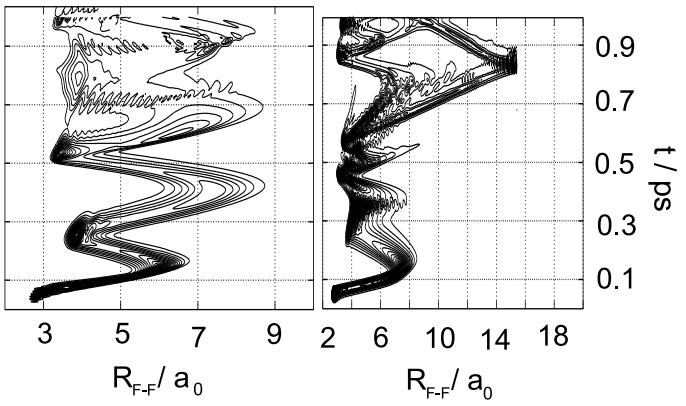

Figure 7.10: Projections of the 2-D wave packets of F_2/Ar onto the $F-F$ coordinate as a function of time, kindly provided by M. Korolkov. Panel a) demonstrates the spreading of the wave packet due to dispersion for the initial condition of a cold window. Panel b) presents the same dynamics for a pre-excited Ar_3 window, leading to partial cage exit of the wave packet at 700 fs.

separation of 11.5 a_0 and the second triangle at 22.9 a_0 and both barriers are saddle points in the 2-D surface (Bohr radius $a_0 = 0.0529$ nm).

The pump pulse prepares the 2-D wave packet on this excited state surface at $R_{FF} = 2.66\ a_0$ and $R_{ArAr} = 4.14\ a_o$ in the well localized ground state configuration. The wave packet moves according to the gradient of the potential surface. It was demonstrated in ref. [72] that the wave packet follows the principle of relief reflection, i.e. the wave packet is reflected by the 2-D walls of the potential (Fig. 7.9a).

Fig. 7.10a shows the projection of the 2-D wave packet onto the $F-F$ coordinate as a function of time for the initial condition of an unexcited Ar_3 window. The originally well localized packet smears out quickly within 1ps. The wave packet is dispersed on the anharmonic potential and the higher dimensionality amplifies the dispersion. In addition, the wave packet will be dephased due to the random encounters with the solvent, which is not considered in the simulation. This explains why oscillations in the pump probe spectra with such pump energies are not observed for longer times. The period in this calculation (~ 250 fs) is significantly shorter than the one derived in the experiment. This is a consequence of the smaller reduced mass of the F_2 compared to ClF, the higher excitation energy used in the simulation and the fact that dissipation to other modes of the Ar lattice is neglected. Fig. 7.10b demonstrates the enhancement of cage exit ($R > 11.5$ a$_0$) for a pre-excitation of the Ar_3 window into its 6^{th} vibrational level. At 700 fs, the additional cage breathing allows part of the wave packet to exit the original cage, which ends at 11.5 a$_0$ on the $F-F$ axis.

There are several drawbacks in this simulation, some of which are discussed in the original work [72, 73]. In addition the P-orbital alignment [68] is not properly taken into account, because of the fixed symmetry in this simulation. As detailed at the end of chapter 5.4.1, the minimum for an aligned orbital is in the center between two and not three nearest neighbor atoms, as assumed in the simulations. Moreover, energy dissipation and coupling to other electronic surfaces is not included and - as will be discussed in chapter 7.5 - the angular reorientation of the fragment is neglected. Nonetheless, the simulations give a good estimate of how the anharmonicity disperses the wave packet and the lower barrier for cage exit when the Ar mode is excited.

7.3.3 Recombination dynamics of Cl_2 in Ar

For Cl_2 the 387 nm pump pulse excites a wave packet with a large excess energy of 8270 cm^{-1}, comparable to the case of ClF in the previous chapter. The expected rapid energy loss is evident from the spectrum at $\lambda_{probe} = 286$ nm (Fig. 6.16), which is the longest probe wavelength, just at the threshold for the $B \rightarrow E$ transition. Here only the first two peaks from the first oscillation period are observed and the spectrum rapidly decays after 1 ps. In the spirit of the discussion in chapters 7.4.1 and 6.2, this indicates that after 1 ps the wave packet has relaxed to the probe window, i.e. it has lost 7000 cm^{-1}. The systematics of this evaluation is given in chapter 7.4.3. The only published

MD simulation [37] on Cl_2 in Ar reports excitation just at the dissociation limit. The first period is 550 fs, which is much faster than the 800 fs seen in the experiment. However, the excitation energy in the experiment is 0.7 eV higher and the deformation of the cage is expected to be larger. The double substitutional site again implies head-on collisions of Cl with Ar. Since the mass of both particles is nearly identical, a complete energy transfer to the Ar atom is expected for a head on collision from classical mechanics. The simulations predicted the generation of shock waves. The dynamics of the belt and breathing modes were already discussed in the context of I_2/Kr (chapter 7.3.1). In the present case the energy transfer to the matrix is even more efficient and coupling of energy back into the Cl_2 mode probably has a significant effect on the dynamics. It would be very helpful to perform MD simulations in the right excitation regime to assign the peaks with certainty. By analogy, the 800 fs period should correspond to the motion in the Cl_2 coordinate and not to the cage breathing, as the signal displays the expected rise of the envelope due to vibrational relaxation. However, the strong modulation in the 286 nm spectrum with the dip at 300 fs probably originates from the cage breathing, as this probe wavelength is just at the threshold.

7.4 Vibrational relaxation kinetics of $I_{2,}$ ClF and Cl_2 in rare gases

7.4.1 Signatures of vibrational relaxation

One unequivocal feature of condensed phase dynamics is dissipation of energy to the bath, which leads to vibrational relaxation of the excited molecule. This process can be displayed by femtosecond pump-probe spectroscopy in several ways. If wave packet oscillations are well resolved and the potential is anharmonic, then the vibrational period is indicative of the mean energy of the wave packet *(method α)*. Thus the relaxation can be monitored by recording the increase of vibrational frequency, while the wave packet is relaxing in the potential well.

A second signature, which is suited also for pump-probe signals in which no oscillations are observed, is the envelope of the pump-probe spectrum *(method β)*. The maximum of the envelope indicates the time, when the vibrational population is relaxed from the initial energy E_{pump} to the energy of the probe window E_{probe}. This is obvious from the classical expression $S \sim 1/v(R_{win})$, which states that the observed signal intensity S is inversely proportional to the velocity v of the wave packet at the probe window R_{win} [27, 45]. The classical expression diverges at the turning point. Similar to the discussion in chapter 2.3.1, this classical expression has its quantum mechanical counterpart in the Franck-Condon overlap of the stationary vibrational wave functions, which remain finite, but are maximal at the turning point. The high probability (large $|\psi(R,t)|^2$) of finding the particle near the turning point in a potential reflects the slow classical motion of a particle in this potential. If the probe window is at the turning point of the wave packet, the packet has zero velocity when it is probed. This corresponds to the antinodes of the vibrational wave functions. Since the wave packet has to continue on the final electronic state with zero velocity, the vertical transition also terminates in an antinode of the final state vibrational wave functions, yielding a large overlap (cf. chapter 5.2.3).

If the wave packet is started at $E_{pump} >´E_{win},$ i.e. above the energy of the probe window (Fig. 2.9), the signal is small initially, because it passes with high velocity v through the window. Vibrational relaxation populates lower levels and the velocity at the window becomes smaller. At the delay time $t = \tau_m,$ when the average energy of the wave packet has arrived in the probe window at $E_{win},$ it is probed at its turning point with zero velocity, and the maximum in the pump-probe signal is observed. The population relaxes further down in the well and the signal decreases, as the wave packet does not reach the probe window anymore [45].

The envelope of the pump-probe spectrum (method β) pictures vibrational population relaxation. It is not sensitive to the coherence of the levels and independent of the question, whether the wave

packet is dispersed, destroyed by collisions, or simply not resolved due to experimental limitations. The disadvantage of method β is that additional information is needed if the excited electronic state is coupled to another state. Then the decay of the signal is a convolution of the population losses to the other state and the vibrational population relaxation. Both methods are compared in chapter 7.4.3 for the example I_2 in Kr and applied to the case of ClF in Ar.

7.4.2 Vibrational relaxation in B state of I_2/Kr from oscillations (method α)

A careful inspection of successive periods in a pump-probe spectrum shows that the period length T_n decreases systematically from the first to the n^{th} oscillation.. For example the pump wavelength $\lambda_{pump} = 520$ nm in Fig. 6.2a yields the successive periods $T_1 = 460$ fs, $T_2 = 410$ fs, $T_2 = 390$ fs, $T_2 = 380$ fs and $T_5 = 370$ fs. The analysis for different pump wavelengths can be found in refs. [32, 144]. A wave packet prepared high up in the B state with a long T_1 falls down in energy by vibrational relaxation. In the time course of relaxation, it passes regions in the B state with increasingly shorter T_n due to the anharmonicity displayed in Fig. 7.1. Thus the change of T_n with delay time can be directly traced to a change of energy E of the wave packet with delay time. For high excitation energies the change in T_n is large enough to read it from the maxima of successive periods in the pump-probe spectrum. For lower excitation, the vibrational relaxation rate decreases (cf. Fig. 7.11) and several periods have to be averaged to obtain high accuracy. The method of a windowed Fourier transformation, introduced by us in ref. [32] to obtain the relaxation rates at low energies, yields the same results. More details are presented in my diploma thesis [144].

The measured rates $k_{rel} = dE/dt$ in cm^{-1} per ps and per period are displayed in Fig. 7.11 (left hand scale). The data set covers a broad range of energies in the B state. A nearly exponential increase is observed, from very low rates with dissipation of only a fraction of a vibrational quantum per period deep in the well ($\lambda_{pump} = 580$ nm) over energy losses of about one quantum per period at $\lambda_{pump} = 540$ nm and to losses of more than 10 quanta per period at and above the gas phase dissociation limit ($\lambda_{pump} = 500$ nm). The smooth change over three orders of magnitude hides that something exceptional happens in the region of the dissociation limit. Fig. 7.11 displays the energy E_1 (dashed line, energy scale to the right) after the first round-trip versus the initial excitation energy E_{pump}. The rise of E_1 with E_{pump} is sublinear, which reflects that the losses per round-trip increase with E_{pump}. Around the dissociation limit, the smooth rise is interrupted, and E_1 falls with E_{pump}. Thus a wave packet that started with a lower energy E_{pump} returns with a larger energy E_1 than a packet that started with initially higher energy. This is not compatible with simple energy and momentum conservation in an elastic scattering event with a cage atom. It indicates that the tremendous losses above the dissociation limit of up to 30 vibrational energies in the first collision are also connected with severe distortions of the cage. These losses are in full accord with the trajectories in chapter 7.3.1.

This evaluation demonstrates that detailed information on potentials and dynamics of a condensed phase system with strong relaxation may be obtained directly from femtosecond pump-probe spectra via method α. The required accuracy for measuring the round-trip time changes considerably with the energy in the B state. Near the bottom of the potential, i.e. for $\lambda_{pump} = 580$ nm, the round-trip time changes by only 4 fs between successive vibrational levels due to the small anharmonicity. In addition it takes about 5 periods to dissipate the energy of one vibrational quantum due to the low relaxation rate. Thus a variation of 4 fs distributed over 5 round-trips has to be resolved and this limits the applicability of the method in this range. However for the interesting case of strong fragment-cage interaction around $\lambda_{pump} = 500$ nm the energy loss per round-trip exceeds 1000 cm^{-1}. The related change of the period on the order of 100 fs is easily resolved.

The consistency of the resulting rates displayed in Fig. 7.11 was checked by comparing a spectrum for E_{pump} with one at the corresponding E_1 (Fig. 7.11), i.e. the energy after one round-trip.. Indeed,

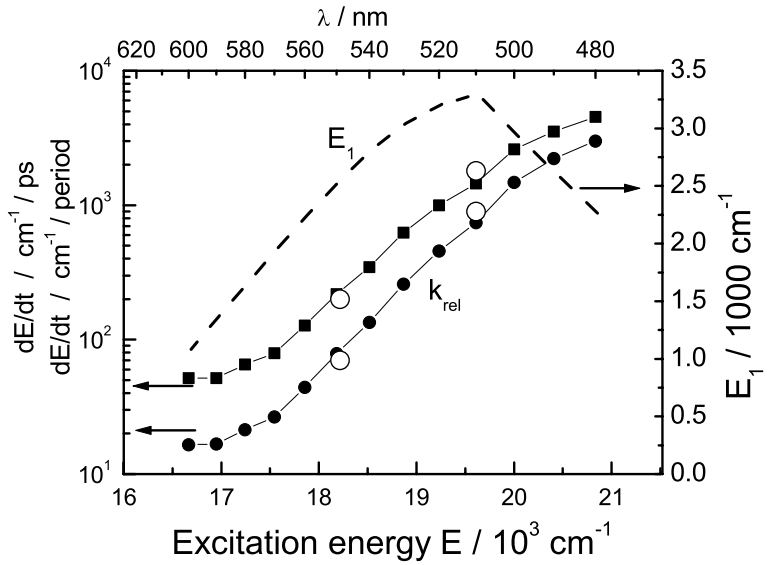

Figure 7.11: Energy relaxation rate $k_{rel} = dE/dt$ of I_2/Kr in the first oscillation as a function of energy in the B state measured in units of cm^{-1}/ps (solid squares) and cm^{-1}/period (solid circles). For comparison the values from ref. [27] are shown as open symbols. To demonstrate that near the dissociation limit the behavior of the system qualitatively changes, the energy E_1 of the wave packet after the first collision (dashed line) is plotted as a function of the initial excitation energy E_{pump}. It shows a maximum around $E = 19500$ cm^{-1}.

perfect agreement is obtained, if the E_1 spectrum is shifted by the period T_1 with respect to the E_{pump} spectrum.

Fig. 7.11 presents the vibrational relaxation rate versus E with a systematic variation over three orders of magnitude. The results are in excellent agreement with the values of the classical simulation in ref. [27] for dE/dt in Kr which are shown as hollow symbols in Fig. 7.11. The values must be read from the graphs in Fig. 6 of ref. [27], because the values given in the text correspond to a rate dE/dt averaged over 1 ps and the present results are averaged over one period only. The small rates near the bottom show up also in the calculations.

7.4.3 Energy dissipation from pump-probe envelope (method β)

B state of I_2/Kr

An alternative signature of the vibrational relaxation is found in the envelope of the pump probe signal (method β). It is discussed first for I_2 and subsequently applied to ClF/Ar and Cl_2/Ar. As it was mentioned above, the maximum of the pump-probe envelope occurs at time τ_m, when the wave packet is probed at its turning point. The difference potential $\Delta V = V_E - V_B$ between the E and the B state (Fig. 7.2) maps the probe wavelength λ_{probe} onto the bond distance R_{win} and the energy E_{win} of the probe window, as it was described in Fig. 7.4. E_{win} is decreased from near the dissociation limit down into the minimum of the B state well by shortening the probe wavelength, i.e. increasing $h\nu_{probe}$. Thus the wave packet is followed during the relaxation and in Fig. 7.12 its energy E_{win} is

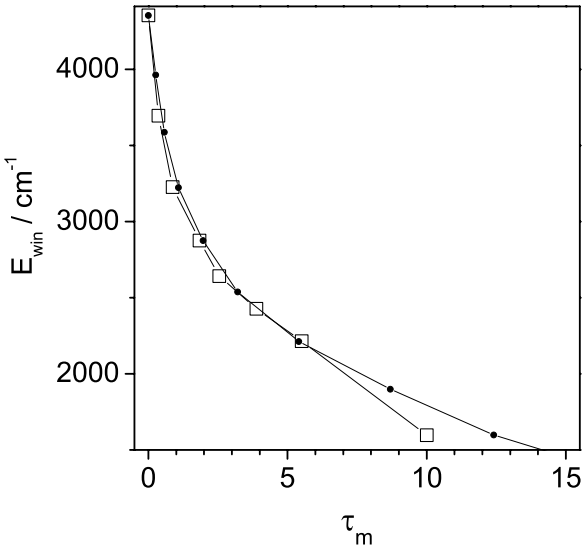

Figure 7.12: The open squares show the energy relaxation as derived from the τ_m values, which are read from the spectra in Fig. 6.4b and collected in Tab. 7.2. Solid dots depict the relaxation as derived numerically from the rates in Fig. 7.11.

plotted as a function of time τ_m. Tab. 7.2 collects τ_m, E_{win} and λ_{probe} for the pump-probe spectra displayed in Fig. 6.4b for a fixed pump wavelength $\lambda_{pump} = 500$ nm. The probe wavelength is varied from $\lambda_{probe} = 530$ nm to 456 nm. The energy of the packet at time $\tau_m = 0$ is taken from the pump wavelength λ_{pump} and the know B state potential[2].

λ_{probe} / nm	τ_m / ps	E_{win} / cm^{-1}
	0	4356
530	0.35	3696
520	0.85	3226
510	1.8	2876
500	2.5	2641
490	3.8	2427
480	5.3	2214
456	10	1597

Table 7.2: Vibrational relaxation of I_2/Kr. Probe wavelength λ_{probe} / nm with the corresponding energy E_{win} in the B state and the related delay time τ_m of maximal intensity in the pump probe spectrum. The excitation at $\lambda_{probe} = 500$ nm corresponds to 20000 cm^{-1} (4356 cm^{-1} above the B state minimum) directly after excitation ($\tau = 0$).

This result can be compared with the relaxation derived from method α. The rates dE/dt in Fig. 7.11 determine the amount of energy $\Delta E_i = t_i dE/dt$,that a wave packet at energy E_i will lose in a time step t_i. The discreteness given by the energies E_i, for which the rates $k_i = dE/dt(E_i)$ have been determined (Fig. 7.11), is used to calculate $t_i(E_i)$ recursively via $t_i = t_{i-1} + (E_{i-1} - E_i)/k_i$. The initial energy is given by $E_0 = E_{pump} = 4356$ cm^{-1} (for $\lambda_{pump} = 500$ nm). The inverse function $E_i(t_i)$ is plotted in Fig. 7.12 as dots, and shows the mean energy of the wave packet starting at E_{pump}. The agreement with the energy relaxation derived with method β (open squares) is excellent . For large delay times, $t > 10$ ps, method β yields times τ_m that are too short. The population losses

[2] $\lambda_{probe} = 540$ nm is not considered in this evaluation, since it lies below the classical resonance, and thus the energy E_{win} is not well defined.

from the B state due to predissociation reduce the signal in addition to the vibrational relaxation. The predissociation time for the B state is larger than 10 ps in this energy region, rendering the envelope a good criterion for energy relaxation at shorter times [115, 116].

A state of I_2/Kr

The A state of I_2/Kr was not studied with systematic variation of the probe wavelength. However, the spectra plotted in Fig. 6.6 already give an estimate for the strong vibrational relaxation in the A state. This state is much more weakly bound than the B state and thus the matrix cage gains importance. The maximum in the dotted curve after $\tau_m = 1.5$ ps indicates that the wave packet has relaxed down to the probe window within this time. $\lambda_{pump} = 670$ nm provides the initial energy $E_{pump} = 3390$ cm^{-1} above the minimum $T_e = 11538$ cm^{-1} of the A state and the probe window for $\lambda_{probe} = 400$ nm is located around $E_{win} = 500$ cm^{-1} above the minimum. Thus the packet loses energy at a rate of approx. 1900 cm^{-1}/ps or 2280 cm^{-1} in the first period of 1200 fs. This loss of $\Delta E/E_{vib} = \Delta E/E_{pump} = 67$ % is included in Tab. 7.4. The energy loss derived here is in excellent agreement with the results of the classical MD simulations presented in Fig. 2.2.

Evaluation for ClF/Ar and Cl_2/Ar

Method β will be used now to derive the energy relaxation in the B state of ClF in Ar from τ_m. The errors due to population losses will be even smaller than in the I_2/Kr case, since the $^3\Pi$ states energetically decouple from all other states for low energies (cf. Fig. 7.19) and the population losses are small. The pump pulse at 387 nm (25840 cm^{-1}) creates a wave packet with an energy of 7400 cm^{-1} above the B state minimum and approx. 5000 cm^{-1} above the gas phase B state dissociation limit. Momentum conservation yields a kinetic energy of about 3000 cm^{-1} in the F fragment [205].

In Figs. 6.8 and 6.9 the Cl^+F^- fluorescence intensity is plotted versus time delay between the pump pulse at 387 nm and probe pulses with wavelengths varying from 322 to 282 nm. The τ_m values are taken from the maxima and are collected in Tab. 7.3. The window location R_{win} and energy E_{win} follow from the difference potential ΔV in Fig. 5.6. $\lambda_{probe} = 320$ nm corresponds to the minimum in ΔV and according to Tab. 7.3 to the probe window position $R_{win} = 0.261$ nm, which lies energetically close to the dissociation limit[3]. Besides the sharp feature near $t = 0$ due to the outward moving wave packet a maximum after a delay time $\tau_m = 1.64$ ps is found (Fig. 6.9). Thus an excess energy of 5780 cm^{-1} is dissipated by strong collisions with the Ar cage during this time and the population has reached the probe energy of 20062.4 cm^{-1} with respect to the X state minimum and 1624.0 cm^{-1} above the B-state minimum (cf. Tab. 7.3).

Dissociation is prevented only by these collisions with the cage and the severe energy loss. The containment of the fragments by the cage is effective and at this energy a cage exit probability of only 4.8 % was derived (chapter 5.4.1). Probing deeper in the well by decreasing λ_{probe} leads to larger τ_m values (arrows in Fig. 6.8 and Tab. 7.3), because it takes longer for the population to reach the energy E_{win} by vibrational relaxation[4]. This flow down in energy of the population versus time τ_m is displayed in Fig. 7.13 by solid squares on a logarithmic scale. The rate of vibrational relaxation is

[3] $\lambda_{probe} = 322$ nm is not considered in this evaluation, since it lies below the classical resonance, and thus the energy E_{win} is not well defined.

[4] A more detailed examination of the envelopes for $\lambda_{probe} = 310$ and 306 nm shows the presence of two maxima, which are due to absorptions to E and f, respectively. In the present evaluation of the vibrational relaxation, only the transitions to the E state were considered. However, the result is not affected much, if for each spectrum the difference potential is used, which has higher weight according to the transition probabilities. Since this change would affect only the evaluation for short wavelengths, where f would be dominant, the determined relaxation rate would be somewhat smaller deep in the minimum, i.e. closer to the Cl_2 result plotted in the same graph (Fig. 7.13 open circles). For Cl_2 no transition moments are available and thus the evaluation can only be made with the E state. The same evaluation has been made for ClF in order have a consistent comparison in Fig. 7.13.

λ_{probe} / nm	R_{win} / nm	τ_m / ps	E_{win} / cm^{-1}
		0	7402.2
320	0.261	1.6	1624.4
318	0.249	1.7	1472.1
316	0.242	1.9	1244.8
314	0.238	2.2	1112.8
310	0.234	3.0	905.0
306	0.230	5.5	735.3
302	0.228	8.9	641.7
298	0.225	13.5	546.1
295	0.223	19.0	468.1
291	0.221	28.0	390.9
288	0.219	35.0	340.2
286	0.218	39.0.	305.8
285	0.218	43.0	288.4
284	0.217	45.0	270.9
282	0.216	54.0	241.4

Table 7.3: Vibrational relaxation of ClF/Ar. Probe wavelength λ_{probe} nm with the corresponding probe window location R_{win} and energy E_{win} in the B state and the related delay time τ_m (Fig. 6.8) of maximal intensity in the pump probe spectrum. The excitation at $\lambda_{probe} = 387$ nm corresponds to 25840 cm^{-1} or 7400 cm^{-1} above the B state minimum directly after excitation ($\tau = 0$).

the slope of the graph in Fig. 7.13. Two distinct regimes of energy dissipation are observed. A large relaxation rate of ~ 3500 cm^{-1}/ps is determined in the early dynamics (inset in Fig. 7.13), when the wave packet is above or close to the dissociation limit and the fragment is only bound by the solvent cage. When the molecule has recombined and is bound by the molecular potential, the relaxation rate has decreased to 10 cm^{-1}/ps.

The same evaluation scheme (method β) is employed for Cl_2/Ar, using the difference potential from Fig. 5.7. The resulting $E(t)$ curve is displayed in Fig. 7.13 by open circles. The Cl_2 molecule initially loses the energy in early dynamics even faster than ClF (inset in Fig. 7.13). The energy loss is $dE/dt \approx 7000$ cm^{-1}/ps. The masses of Cl and Ar are 39 and 40 amu, respectively, and from classical billiards it is evident that this leads to a very effective energy transfer in a head-on collision, which Cl fragments experience when dissociated on a double substitutional site (chapter 2.2.1). This corresponds nicely with the discussion in chapter 7.3.3, where the same rapid relaxation is also evident from the oscillation pattern.

Comparison of ClF/Ar, Cl_2/Ar and I_2/Kr

If the results for the energy relaxation in the B state of ClF/Ar and Cl_2/Ar (Fig. 7.13) are compared to those in the B state of I_2/Kr (Fig. 7.11), it catches the eye that the decay is much smoother in the latter case (a logarithmic energy scale would even decrease the curvature). The main reason is that I_2/Kr is excited just at the gas phase dissociation limit, whereas ClF/Ar and Cl_2/Ar are pumped far beyond. The energy loss in the first ps is large and the wave packet quickly drops below this limit. Within the bound part of the molecular potential the interaction with the matrix is much smaller.

Fig. 7.14 shows a comparison of the relaxation rates dE/dt for ClF/Ar, Cl_2/Ar and I_2/Kr as a function of the excess energy E_{excess} above the gas phase dissociation limit. The rates for ClF/Ar (open circles) and Cl_2/Ar (open squares) are the derivative of the $E(t)$ curves from Fig. 7.13 (method β). For I_2/Kr (solid squares) they are reproduced from Fig. 7.11, where they are derived from the

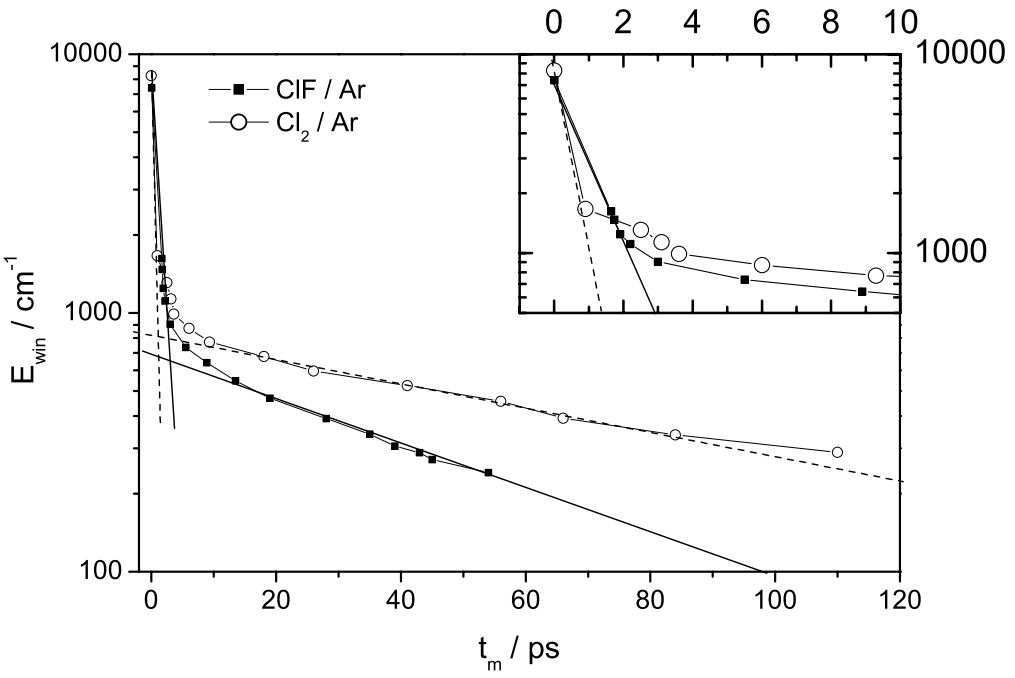

Figure 7.13: Vibrational energy E_{win} in the B state versus delay time τ_m, obtained from the maxima of the pump-probe spectra in Fig. 6.8 for ClF/Ar (solid square) and in Fig. 6.15 for Cl_2/Ar (open clircles).

vibrational periods (method α). The equivalence of the two methods was shown in chapter 7.4.3. For negative excess energies E_{excess} in Fig. 7.14, the molecules are bound in the molecular potential. The horizontal lines near $E_{excess} = 0$ correspond to an energy loss of 100% of the energy above the potential minimum E_{vib} in one collision for I_2/Kr (dash) and ClF/Ar (solid)[5]. This is the maximal rate in the picture of an oscillating wave packet. The measured rates indeed approach this limit exponentially and turn over to the limiting slower increase near the dissociation limit $E_{excess} = 0$.

The nonlinear increase of the relaxation rates is related to the soft anharmonic potential, which allows large bond extensions at high vibrational energy E_{vib} of the molecule. At the gas-phase dissociation limit ($E_{excess} = 0$) the bond length would already reach far beyond the size of the matrix cage, if the molecules were not confined by the forces imposed by the surrounding rare gas atoms. Therefore, the coupling of the molecule to the matrix cage becomes very strong.

The high rates for the energy loss per picosecond have to be used with care. The periods are shorter than 1ps, and the microscopic picture suggests that the energy loss takes place per collision rather than in a continuous way. Recall the peculiar consequence of the nonlinear increase of the energy dissipation that was derived for I_2/Kr (Fig. 7.11). There it was demonstrated that excitation at higher energy E_{pump} may lead to a lower energy E_1 after the first collision (cf. 7.6). Fig. 7.14 shows that for I_2/Kr at the dissociation limit ($E_{excess} = 0$), the rate is $dE/dt = 2600$ cm^{-1}/ps. Since one oscillation takes 570 fs, the energy loss in the first round-trip is 1480 cm^{-1}. In the collision the rate will be only $dE/dt = 400$ cm^{-1}/ps for the lower $E_{excess} = -1480$ cm^{-1}.

As a survey, Tab. 7.4 displays the fraction (percentage) of energy $\Delta E/E_{vib}$ lost in one period T for selected excess energies E_{vib} and for several electronic states. The periods are taken from the wave packet dynamics in chapter 7.3, except the values for ClF and Cl_2 near the minimum, which

[5]For Cl_2/Ar this limit is intermediate between ClF/Ar and I_2/Kr.

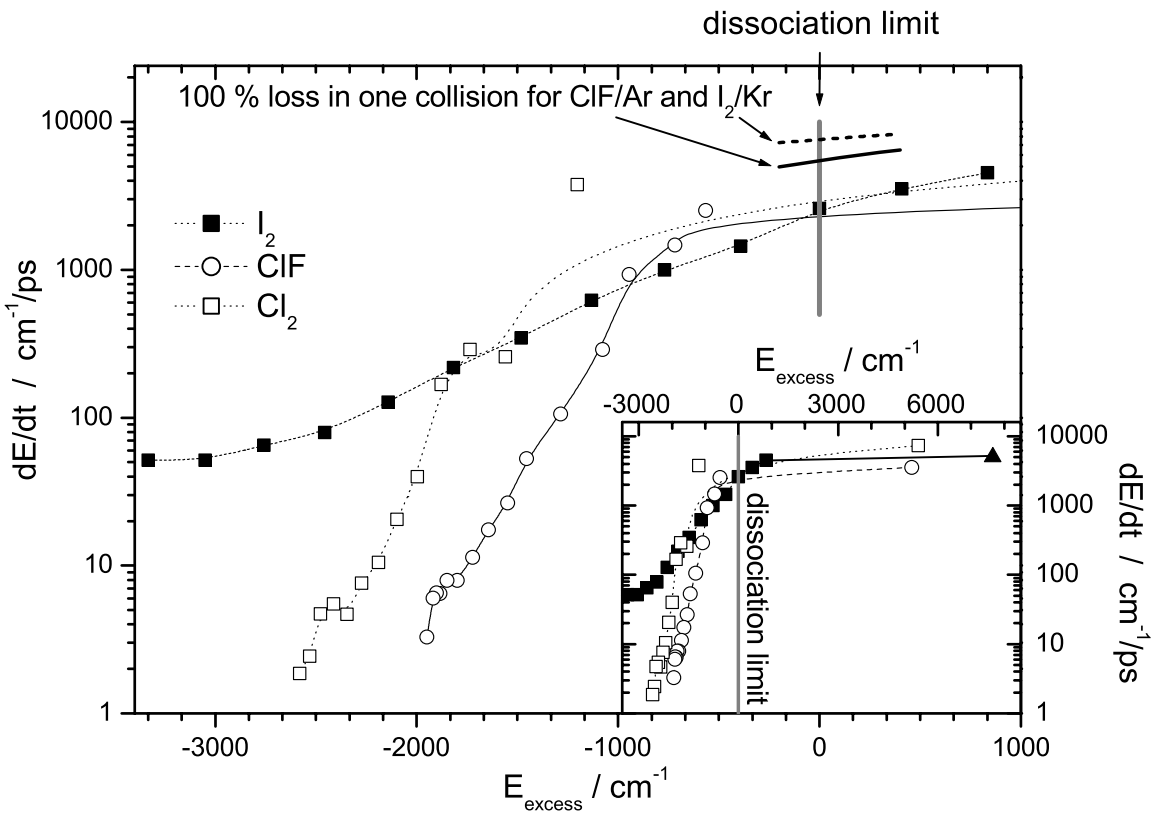

Figure 7.14: Relaxation rates dE/dt for I_2/Kr (solid squares), ClF/Ar (open circles) and Cl_2/Ar (open squares) as a function of the excess energy E_{excess} above the gas phase dissociation limit. For all three molecules the rates increase exponentially in the bound region ($E_{excess} < 0$). They approach the maximal rate of 100% loss per period (solid line for ClF/Ar, dashed for I_2/Kr) near the dissociation limit. The inset includes the large rates far beyond the limit. The solid triangle corresponds excitation of I_2/Kr to its B'' state.

	I_2/Kr			ClF/Ar		Cl_2/Ar		units
state	B	A	B''	B	$^1\Pi$	B	$^1\Pi$	
D_0	4350	1650	0	2190	0	2870	0	cm^{-1}
High vibrational energy								
$\Delta E/E_{vib}$	**57**$\pm$5	**67**$\pm$20	**70**$\pm$20	**35**$\pm$10	**55**$\pm$20	**60**$\pm$20	**60**$\pm$20	**%**
E_{excess}	830	1750	7650	5210	17200	5410	18080	cm^{-1}
E_{vib}	5180	3400		7400		8280		cm^{-1}
$T(E_{vib})$	660	1200	1200	675	675	800	800	fs
Low vibrational energy								
$\Delta E/E_{vib}$	**1**$\pm.5$			**0.2**$\pm.1$		**0.1**$\pm.1$		**%**
E_{excess}	-3050			-1890		-2470		cm^{-1}
E_{vib}	1300			300		400		cm^{-1}
$T(E_{vib})$	315			100		130		fs

Table 7.4: Vibrational relaxation in ClF/Ar, Cl_2/Ar and I_2/Kr for excitation to different electronic states. The energy loss $\Delta E/E_{vib}$ in percent is given for high and low vibrational energies. The confidence intervals are estimated from the uncertainty of the vibrational period and energy loss. If the excess energy E_{excess} is negative, the molecule is bound by its own potential and the rate is very small. For excitation above the gas phase dissociation limit, about half of the energy is lost in the first period.

are from the spectroscopic data for the gas phase from ref. [206]. Intermediate relaxation rates can be read from Fig. 7.14

7.5 Depolarization and angular reorientation

This chapter presents one of the few examples where ultrafast angular reorientation of molecules in the condensed phase has been detected with femtosecond pump-probe spectroscopy. It offers for the first time the possibility to compare the ultrafast decay of the polarization anisotropy to the sophisticated DIM-trajectory calculations.

7.5.1 Ultrafast reorientation of molecules measured by polarization dependent pump-probe spectroscopy

In the ultrafast dissociation-recombination events examined in this thesis, the scattering of the fragments off the solvent cage atoms may be asymmetric and lead to recombination in a tilted geometry (Fig. 7.15a). Polarization dependent femtosecond pump-probe spectroscopy is exploited to measure this reorientation[6] of the recombining fragments in time during the first encounters on the ultrafast timescale, which is dictated by the kinetic energy of the fragments and the fast dissipation of rotational and vibrational energy in condensed media. Starting from a sample with randomly oriented molecules, a linearly polarized pump pulse prepares an anisotropic ensemble of excited state molecules (photoselection) [140] and dissociates them. The anisotropy is probed during the recombination process with a second linearly polarized pulse by recording the laser induced fluorescence.

Although it is well known that such polarization sensitive measurements yield information on the rotational motion of molecules according to the selection rules for electronic transitions, only few experiments used this method on an ultrafast timescale. The rotation of free molecules and the coherent vs. random rotation of I_2 in liquid rare gases [216, 217] has been displayed by this method and it was proposed to measure the fragment rotation for ICN in liquid Xe [218]. Often these polarization effects are neglected or unwanted and the experiment is performed in the magic angle

[6] In this chapter the words "reorientation" and "orientation" are used as the colloquial form of the word alignment. It does *not* imply orientation of an arrow, i.e. with direction.

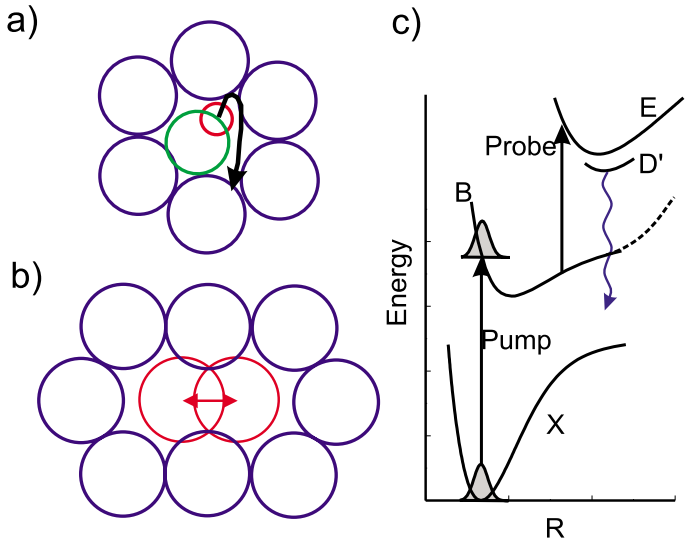

Figure 7.15: a) Scheme for a ClF molecule on a single substitutional site in an Ar matrix. After photodissociation the F fragment can be scattered into a new orientation with respect to Cl, depending on the scattering parameters. b) Scheme for an I_2 molecule on a double substitutional site in a Kr matrix. The geometry suggests that tilting the molecule is strongly inhibited. Dissociation leads to vibrational motion after recombination. c) Pump-probe scheme for both molecules with the relevant electronic potential curves.

configuration to be sensitive to vibrational wave packet dynamics only [21]. A different approach uses polarization effects in the third order polarizability with techniques like CARS or Kerr-effect [22,219].

For the polarization sensitive measurements in chapters 6.1.2 and 6.3.2 the following scheme was used and the first five lines of Tab. 2.3.5 are relevant. Starting from the vibrational ground state $X(^1\Sigma_0)$ in both cases (Fig. 7.15c), the $B(^3\Pi_0)$ state $(\Delta\Omega = 0)$ is excited with the linearly polarized pump pulse, creating a $\cos^2(\Theta)$ distribution of excited molecules aligned with the laser polarization. The time delayed probe pulse transfers population to the $E(^3\Pi_0)$ state and after relaxation within the ion-pair manifold, emission from the $D'(^3\Pi_2)$ state is observed [80, 115, 205]. The transitions between valence and ion-pair states obey the selection rule $\Delta\Omega = 0$ favoring an electric field parallel to the internuclear axis. The probe pulse has horizontal polarization in all experiments and the pump pulse is polarized either parallel $(\ \|\ )$ or perpendicular $(\perp)$ with respect to the probe polarization. In the pump-probe experiments, the fluorescence from D' is collected in forward direction without polarization sensitive optics (first three lines in Tab. 2.3.5). To check the results, a polarization analyzer is introduced (lines four and five in Tab. 2.3.5).

Tab. 2.3.5 summarizes the intensity ratios for the probe absorption of an ensemble photoselected by the pump. $I_\|$ and $I_\perp$ in the last column are the ratios for completely preserved photoselection parallel and perpendicular to the probe polarization. I_d denotes probing a depolarized (random) distribution with linearly polarized light. If the laser induced fluorescence (LIF) is detected without polarization sensitive optics, it is proportional to these ratios. lines four and five indicate the intensity ratios observed, if a photoselected ensemble is probed with polarization parallel to the selected axis and the LIF is detected with a parallel ($I_{LIF\|}$) or perpendicular ($I_{LIF\perp}$) polarization analyzer. An interchange of analyzer and probe polarization yields the same ratio for symmetry reasons.

The classical trajectory calculations summarized in chapter 2.1 show that scattering of F fragments in the Ar cage can lead to recombination of F_2 with a tilted bond direction (Fig. 2.4). The fragments are small enough to move inside the nearly isotropic cage (Fig. 7.15a). These skewed scattering events also appear in nonadiabatic trajectory calculations (Fig. 7.17 [71]). However, for I_2/Kr such events are not expected because of the geometry of the double substitutional site, occupied by the I_2 molecule (Fig. 7.15b). Accordingly, reorientation of the bond is not observed in the corresponding classical and semiclassical simulations of I_2/Kr. To demonstrate the different behavior of I_2/Kr vs. ClF/Ar, the same set of experiments is performed on both systems in the way described above. Both molecules have similar electronic structure. The nonadiabatic dynamics on several electronic states are discussed in chapter 7.6, which deals with the dynamics of spin-flips. The method of polarization

dependent pump-probe spectroscopy applied in the following separates out the geometric orientation only.

7.5.2 Sterically fixed molecule: I_2/Kr

The spectra in Fig. 6.5 for I_2/Kr and $\lambda_{pump} = \lambda_{probe} = 486$ nm with parallel (solid) and crossed (dashed) pump-probe polarization show an oscillatory structure from the vibrational wave packet dynamics. The I_2 wave packet prepared 0.08 eV above the dissociation limit dissipates 0.44 eV within 1 ps according to the rates in Fig. 7.11, leading to the increasing envelope function. The fact that both spectra in Fig. 6.5 coincide perfectly after multiplication of the parallel spectrum by the factor $1/3$ for preserved photoselection (cf. Tab. 2.3.5) implies that the I_2 molecule is indeed fixed in space as expected from the axial symmetry of the tight Kr cage around the double vacancy. This is indicated in Fig. 7.15b.

The results confirm that unlike the results for I_2 in liquid Kr [216, 217], the angular reorientation (randomization) of the I_2 molecule embedded in a solid Kr matrix is negligible, since it is inhibited by the rigid matrix cage despite the large amount of energy deposited locally. In high pressure Ar at room temperature, on the contrary, the anisotropy depicts the coherent rotational motion of I_2, that leads to a dip after 2 ps, and a constant asymptotic anisotropy of 0.1 at low pressures [217]. For high pressures approaching liquid phase densities, the random collision time becomes faster and faster, until the rotational coherence is destroyed and the anisotropy decays to zero.

At $\lambda_{pump} = 486$ nm the B'' state is also populated and this transition ($\Delta\Omega = 1$) selects an ensemble perpendicular to the polarization. However, only the B state is probed in this experiment and the small portion of the wave packet crossing from B'' to B is negligible according to experimental observation in ref. [115, 116]. For low excitation, it may suffice to perform an experiment with a single linearly polarized pulse that excites the B state and to measure the polarization of the $B \rightarrow X$ fluorescence [33], to prove the preserved alignment. If I_2 is excited above 500 nm, the $B \rightarrow X$ fluorescence originates from both $^1\Pi_1$ and $B(^3\Pi_0)$ excitation. In that case one can *assume* that the molecule is not tilted and use the polarization of the fluorescence to separate $^1\Pi_1$ and $B(^3\Pi_0)$ as it was done for ICl in Ar [220]. Moreover, in order to compare to ClF/Ar, the pump-probe experiment is required to be sensitive to angular reorientation of the molecule in the excited state on the fs-timescale.

7.5.3 Random scattering in cage: ClF/Ar

Fig. 7.16a reproduces the spectra from Fig. 6.10 ($\lambda_{pump} = 387$ nm and $\lambda_{probe} = 317$ nm) with parallel ($\parallel$ solid line) and perpendicular ($\perp$ dashed line) pump-probe polarization. Directly after excitation ($t = 0$) the ratio of the recorded fluorescence intensities is close to the expected ratio of $I_\perp/I_\parallel = 1/3$ for preserved photoselection. After 2 ps both spectra coincide, indicating complete depolarization. The oscillatory structure reflects the wave packet dynamics. $I_\parallel$ at $\tau = 0$ is scaled to the value 0.6. Then $I_\perp(t = 0)$ is close to the 0.2 in accordance with Tab. 2.3.5 for preserved photoselection. For the complete depolarization, reached after 2 ps, one would expect $I_\parallel = I_\perp = 0.33$. However, the observed signals converge to the value of 0.5. The reason for the difference is ultrafast vibrational relaxation of ClF in Ar. The ClF wave packet prepared 0.6 eV above the dissociation limit relaxes below the dissociation limit within 1 ps. The larger probe efficiency yields the increase of the signal for both polarizations (chapter 7.4.3). To eliminate the changes due to the probe efficiency, the anisotropy $r = (I_\parallel - I_\perp)/(I_\parallel + 2I_\perp)$ is calculated. Fig. 7.16b shows the anisotropy $r(t)$ together with an exponential fit $r(t) = r_0 \exp(t/\tau_r)$ with the time constant $\tau_r = 1.2$ ps and an initial value of $r_0 = 0.35$, close to the expected value of 0.4. The exponential decay to $r(t > 2ps) = 0$ indicates complete depolarization. Thus τ_r is the timescale for randomization of the molecule's orientation induced by dissociation, scattering of fragments off the cage and subsequent recombination.

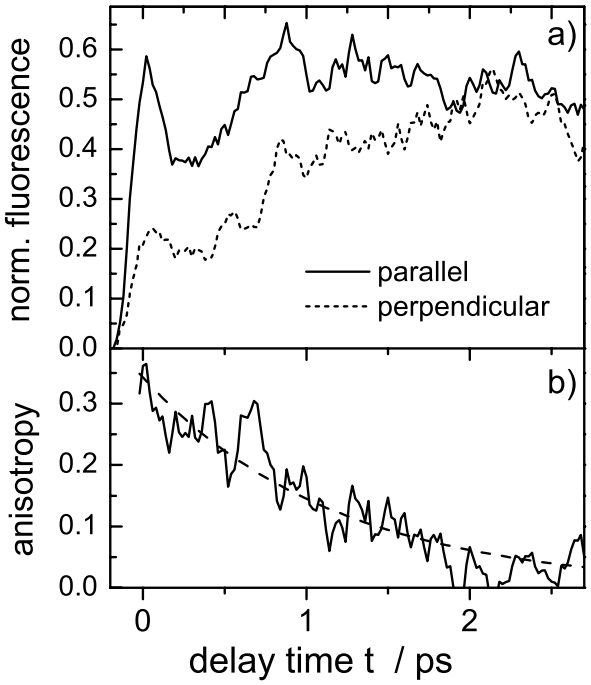

Figure 7.16: a) fs-pump-probe spectra with $\lambda_{pump} = 387$ nm and $\lambda_{probe} = 317$ nm for ClF in Ar from Fig. 6.10. The spectra for $\parallel$ and $\perp$ pump-probe excitation converge after 2 ps but show a ratio of nearly $I_\perp/I_\parallel = 1/3$ directely after excitation. b) The anisotropy $r = (I_\parallel - I_\perp)/(I_\parallel + 2I_\perp)$ is shown together with an exponential decay with the time constant $\tau_r = 1.2$ ps. The depolarization proves the ultrafast statistical angular reorientation of the ClF molecule.

The time $\tau_r = 1.2$ ps should be related to the vibrational period (400 fs) of ClF and the Ar-cage-breathing mode (800 fs) discussed previously (chapter 7.3.2) [205]. The first fragment-cage collision leads to a dramatic loss of kinetic energy in the ClF. From this point of view, it is surprising that the angular randomization in the first 500 fs is rather small (cf. Fig. 7.16b). The anisotropy decreases from $r_0 = 0.35$ to 0.25. The data suggest that the cage breathing which is induced by the impulsive first collision enforces the tilting of the molecular bond after 800 fs.

The results discussed above have several important implications. It is demonstrated experimentally for the first time that fs-pump-probe spectra of small molecules in condensed phases $-$ even in a rigid matrix cage $-$ display fast depolarization. In the future this method can be used to measure molecular alignment on the femtosecond timescale induced by strong non-resonant IR pulses. These experiments are in preparation. It is confirmed that the validity of reduced dimensionality approaches [72,73], which keep the internuclear bond orientation fixed and propagate 2-D wave packets quantum mechanically, is limited to the first oscillation. The experimentally determined decay of the anisotropy can be compared to the statistics of trajectory simulations, once the averaging of the trajectories is accomplished. Again this signature is very useful, since the tedious calculation of the ion-pair potentials is circumvented, and the pump-probe spectrum itself need not be simulated.

Mechanism

The timescale of angular reorientation can be compared to high level trajectory simulations in the spirit of the DIM formalism [71]. In this way predictions for the scattering of open-shell fragments [68, 70] and recombination onto excited molecular states can be verified experimentally. The information on depolarization is contained in the calculations [71] (Fig. 7.17). An evaluation presenting an average over the trajectories like for the spin-flip transitions (see below) is missing, although highly desirable.

The mechanism that induces angular randomization can be deduced from the simulations, which were carried out for the similar situation of F_2 dissociation at different levels of sophistication. The classical molecular dynamics calculations that used isotropic $F - Ar$ potentials [67] were improved

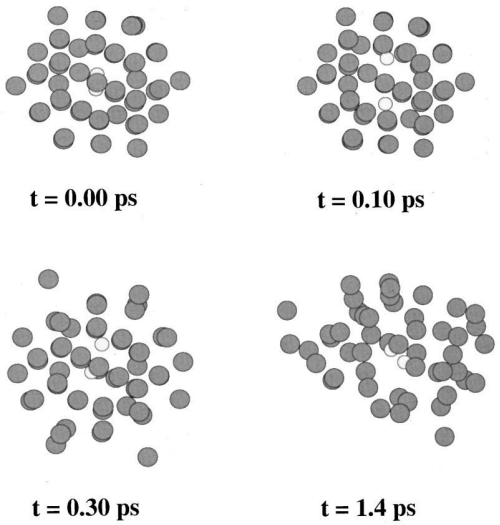

Figure 7.17: Snapshots of the molecular dynamics of F_2/Ar_{54} from ref. [71]. The balls represent F atoms (white) and Ar atoms (grey). In the first 300 fs, the molecular bond is broken and recombined again in the initial orientation. After 1.4 ps the bond is tilted by more than 50°.

by explicitly taking into account the open-shell nature of the fragments [68, 70] and by a full DIM-simulation[7] including nonadiabatic effects [71]. For illustration consider Fig. 7.17 taken from ref. [71], which shows snapshots of a typical trajectory of F_2 in an Ar_{54} cluster with excitation parameters close to our experiment. In the first 300 fs, the $F-F$ bond is broken and formed again in the original orientation. After 1.4 ps, however, the bond is tilted by more than 50°. Obviously, a time dependent orientation averaged over all trajectories would be more informative than this single trajectory.

A more detailed discussion of the microscopic structure shall be given, that describes important features of the problem. The ClF molecule is supposed to be aligned in the way depicted in Fig. 2.5, i.e. with the fragments pointing symmetrically at the triangular windows. The discussion of the molecular orbitals in chapter 2.4.5 showed, that the P-orbital of the dissociating F atom will be aligned with the direction of motion (Fig. 2.14). As already mentioned, ref. [68] showed that in this geometry the barrier for dissociation is 2.1 eV with the saddle point in the center of the Ar_3 triangle, symmetrical to the dissociation. The P-orbital will align with the plane of the Ar_3 triangle after dissociation, because then the barrier is lowered to 0.7 eV. The saddle point now lies in the center between two Ar atoms, i.e. asymmetrical to the direction in which the F fragment was dissociated. It is evident that the corresponding potential surface will enforce a skewed scattering event. On the other hand, since there are three saddle points which are symmetrically ordered around the axis of dissociation and correspond to different alignments of the orbital, the problem remains symmetrical until the symmetry is broken and the Jahn-Teller effect is established. It will be a challenge to future experimental and theoretical studies to decide how fast the P-orbital is aligned by the cage forces [68–70].

7.6 Solvent induced spin-flip

This chapter presents the perhaps most surprising result of these studies. Pump-probe signals evidence the ultrafast spin-flip in ClF induced by the presence of the solvent. Cl and F are light atomic fragments, and in the gas phase the intersystem crossing is forbidden on a nanosecond timescale.

Great effort is taken to investigate the non-adiabatic coupling in molecules, i.e. the interplay of the dynamics of electrons and nuclei in the presence of the solvent. The spin-selection rule in molecules composed of light atoms is strict and intersystem crossing is intuitively considered to be slow.

[7] Similar calculations on ClF/Ar are currently pursued in the group of Prof. Manz.

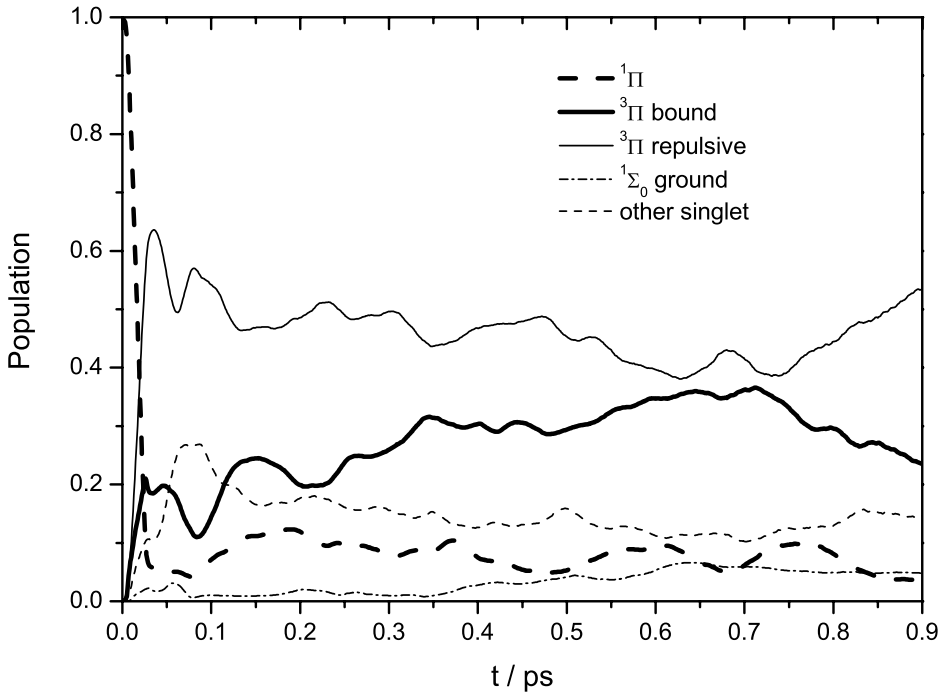

Figure 7.18: Populations of electronic states after excitation to the singlet state ($^1\Pi$) of F_2/Ar_{54} ensemble averaged over many trajectories in ref. [71]. The lines indicate the populations in the initially excited singlet state ($^1\Pi$) (thick dashed), the bound triplet states ($^3\Pi$) (thick solid), all repulsive triplet states (thin solid), the ground state (thin dash-dot) and all other singlet states (thin dashed). After 60 fs, the population in all triplet states is 0.8, which is the statistical weight of the triplet states. The growing population in the bound triplet states (thick solid) is observed in the experiment (cf. Fig. 7.21).

Strong transitions are observed in light diatomics from the ground state $^1\Sigma_0$ only to the singlet states, e.g. $^1\Pi_1$. The absorption cross section to the triplet states is much smaller according to the spin selection rule. The $B(^3\Pi_0)$ state can be accessed in the experiment by appropriate spectral selection (cf. Fig. 5.2).

Recent simulations of nonadiabatic dynamics in the excited states of F_2 in Ar clusters predicted that ultrafast spin-flips play an important role in the dynamics and occur on the 100 fs timescale [71]. The same has been calculated for HCl in Ar [221, 222]. The second important prediction is the rapid recombination of the molecule into different excited electronic states as opposed to recombination into the original state or into electronic ground state. These non-adiabatic transitions have been investigated in detail for the similar system of I_2 in rare gas both theoretically [63, 64, 66] and experimentally [27, 46, 115]. Strong spin-orbit coupling in I_2 already weakens the spin selection rule in the free molecule. The small spin-orbit interaction in the case of ClF or F_2 molecules simplifies the potential diagram, and the solvent contribution to the spin-flip can be demonstrated more clearly. It is important to keep in mind that non-adiabatic coupling between a pair of electronic states is bidirectional, i.e. the wave packet hops back and forth with equal probability. In the following discussion it will be shown that in the condensed phase it is the energy dissipation to the surrounding that directs the process towards lower energy [115].

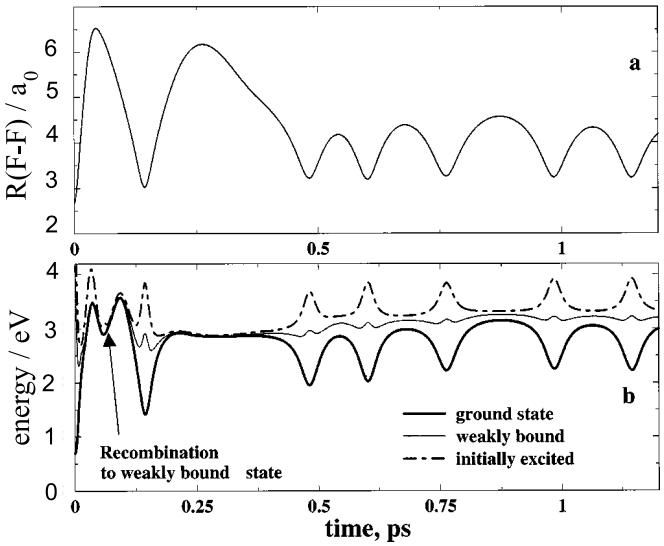

Figure 7.19: Single DIM-trajectory demonstrating the mechanism of spin-flip from ref. [71]. After 60 fs, the trajectory hops from the initially excited $^1\Pi$ to a bound triplet state. In the next excursion it loses so much energy to the solvent that the electronic states decouple, i.e. the trajectory does not reach the region at large R where the states overlap. It is trapped in the bound triplet state.

7.6.1 Spin-flip in F_2 (theory)

First the theoretical findings that stimulated the measurements shall be summarized. In the simulations [71] of F_2 in Ar_{54} clusters the electronic states were described by the valence bond approach for the $F(^2P) + F(^2P)$ interaction. The spin-orbit and non-adiabatic coupling was included and the anisotropic interactions between $F(^2P)$ and Ar are described by the diatomics-in-molecules approach (DIM). This basis was used throughout to construct the 36 electronic valence states. The dynamical simulations use the surface hopping method. The study analyzed photodissociation and recombination dynamics. The present investigation focuses on the ultrafast spin-flip in the recombination dynamics of ClF in Ar. Hence only the main results concerning the recombination of F_2 in Ar with comparable photoexcitation at 4.6 eV are summarized Fig. 7.18. The data were kindly provided by M. Niv.

The molecule is excited into the $^1\Pi_1$ state by an ultrafast laser pulse. The trajectories move outwards, and preferentially at large bond distances, surface hopping to other electronic states occurs. The population of the initially excited singlet state $^1\Pi$ (thick dashed line), drops from unity to 0.1 within less than 40 fs and subsequently remains nearly constant within the simulated time of 1 ps. The population is transferred to the bound (thick solid line) and repulsive (thin solid line) triplet state in the first 40 fs. Slightly later ~ 60 fs, the other singlet states gain some weight (thin dashed line). Subsequently, the main process is transfer of population from the repulsive triplet and singlet states to the bound triplet states $^3\Pi_u$. 40% of the population accumulate in the bound triplet states in the first 700 fs, and subsequently population is partially transferred back to the repulsive triplets. The interpretation in ref. [71] is that after 60 fs the trajectories are distributed among the triplet and singlet states with the statistical weight of 3:1. A reason for the accumulation in the bound triplet states is found in the corresponding trajectories. Fig. 7.19, reproduced from ref. [71], shows a trajectory that hops to the bound triplet state after 100 fs. The bound triplet state is depicted by the thin solid line. In the subsequent excursion of the trajectory to large $F - F$ distances (upper panel), a lot of energy is dissipated to the Ar atoms, and the bound triplet states "decouple" from all other states, since the trajectories no longer reach the region where the states cross.

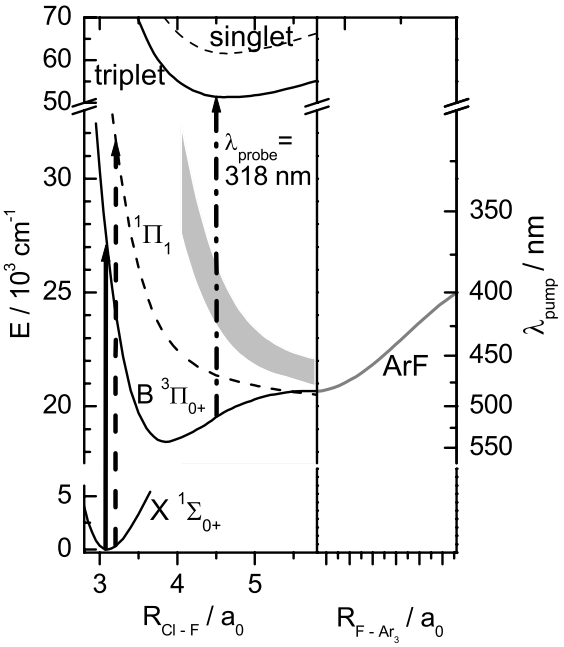

Figure 7.20: One dimensional potential diagram of the ClF molecule embedded in an Ar matrix. The left panel reproduces the gas phase potential energy curves for ClF taken from ref. [121]. The right panel schematically shows the cage-effect of the surrounding Ar crystal, that imposes a binding force on the fragments, here represented by the ArF potential. The following valence states of the ClF molecule are shown: Ground state $X(^1\Sigma_{0^+})$, the $B(^3\Pi_{0^+})$ state as a representative of all four bound $^3\Pi$ states which coincide within 500 cm^{-1}, the repulsive singlet $^1\Pi_1$, and the gray shaded area covering all other valence states. The ion-pair manifold contains the closely spaced triplet states $^3\Pi$ and $^3\Sigma$. The singlet states lie 10000 cm^{-1} higher in energy and cannot be accessed with the wavelenghts used in this experiment.

7.6.2 Spin-flip in ClF (experiment)

In the following these theoretical studies are compared to experimental findings derived from fs-pump-probe spectra on ClF/Ar. The discussion will show that there is good agreement on the fact that population accumulates in the bound triplet states shortly after singlet excitation. The ultrafast spin-flip and the large amount of recombination onto bound excited states are verified.

The bound triplet states $^3\Pi_\Omega$ are probed via the strong charge transfer transitions to the ion-pair states $^3\Pi_\Omega$, and for the chosen probe wavelength $\lambda_{probe} = 318$ nm these are the only energetically accessible transitions (cf. Fig. 7.20). The fluorescence intensity at 420 nm is recorded versus time delay. The states with $\Omega = 0, 1$ and 2 are very closely spaced due to the weak spin-orbit interaction and we do not attempt to separate them. In the F_2 molecule they correspond to the $^3\Pi_u$ manifold. Two different pump laser beams ($\lambda_{pump} = 280$ nm and $\lambda_{pump} = 387$ nm) are overlapped on a dichroic mirror and focused together with the probe beam onto the sample (chapter 6.3.3 and Fig. 6.11). By blocking one of the two pump beams one can now choose to excite the ClF molecule either to the singlet state $^1\Pi_1$ (280 nm) or to the triplet $B(^3\Pi_0)$ (387 nm). Fig. 7.21a shows the pump-probe spectra obtained by delaying the probe pulse by the time t with respect to the pump. Direct excitation to the $B(^3\Pi_0)$ state (solid curve), produces the oscillations due to vibrational dynamics of the wave packet discussed in chapter 2.1.5. The first maximum at $t = 50$ fs corresponds to probing the wave packet on the outward stretch motion ($\rightarrow$) of the $Cl - F$ bond. The peak at $t = 500$ fs indicates the return of the wave packet ($\leftarrow$) into the probe window after it has lost almost half its kinetic energy (~ 0.6 eV) with respect to the minimum of the B state [195]. In the next two maxima the packet is probed near its turning point ($\leftrightarrow$) with the vibrational period of 300 to 400 fs, typical of ClF in the B state near the dissociation limit.

If on the other hand, the molecule is excited into the singlet state $^1\Pi_1$ (dashed curve), the pump-probe signal is close to zero at time $t = 0$, since only the triplet states $^3\Pi$ are probed. However, the spectrum rises, indicating population transfer to $^3\Pi$, i.e. spin-flip, and it converges to the pump-probe spectrum for direct excitation into $B(^3\Pi_0)$ within 1.5 ps. The wave packet dynamics, displayed by

the oscillations in the signal, are similar and interpreted in the same way, except for a larger energy loss than for triplet excitation. This energy loss, qualitatively compatible with the simulations [71], is on the order of 1.5 eV due to the higher kinetic energy that the Cl and F fragments attain by excitation with $\lambda_{pump} = 290$ nm. In the preceding chapters it was shown that energy dissipation increases nonlinearly with excitation energy in ClF and in the analog system, I_2 in Kr solid [27,46]. The inset in Fig. 7.21 shows that the spectra agree for all delay times longer than 2 ps within the reproducibility. Shorter probe wavelengths displayed in Fig. 6.11 display the B state population deeper in the well with lower vibrational excitation and the signal can be observed up to 100 ps. At these long time delays the spectra for excitation to singlet $^1\Pi_1$ or to triplet $B(^3\Pi_0)$ coincide perfectly and the spectra are normalized accordingly. The normalization constant accounts for the different absorption coefficient and photon flux. The oscillations in the early part of the signals display the wave packet dynamics as described before and the envelope shows the signature of vibrational relaxation. At first the signal increases, as the wave-packet relaxes into the probe window, improving the Franck-Condon overlap with the ionic states. Then the intensity decreases as the wave packet energetically falls out of the probe window.

As a measure of the spin-flip, the ratio of the dashed ($I_{\sin glet}$) and the solid ($I_{triplet}$) curve from Fig. 7.21a, i.e. $I_{\sin glet}/I_{triplet}$ is plotted in Fig. 7.21b as the solid line. It represents the triplet population after singlet excitation normalized to that for triplet excitation. The division by $I_{triplet}$ removes most of the variation of the detection sensitivity with delay time caused by vibrational relaxation. To derive the spin-flip rate from the experimental data, the increasing population is fitted with an exponential growth (dotted line), $I_{flip}(t) = 1 - \exp(-t/\tau_f)$, with a time constant $\tau_f = 500$ fs as the only adjustable parameter. However, the spin-flip seems to occur preferentially at times when the ClF bond is stretched, according to the step in the experimental solid line between 250 and 400 fs. At time $t = 0$ the triplet population must be zero, and the small finite value measured in the experiment is due to the finite duration (100 fs) of the laser pulses. The chosen scale in Fig. 7.21b agrees with the fraction of molecules predicted to cross to the bound triplet states in the simulation [71]. In the simulations, there are also dissociated molecules with fragments that left the cage and large $Cl-F$ distance, which are not included in the present count. The triplet state population accumulated according to the simulation is displayed in Fig. 7.21b as open circles[8]. The agreement of experiment and theory is excellent. The scatter in the theoretical data reflects the statistics of the trajectories, while the bleaching of the sample limits the time to accumulate experimental data.

A correction of the spectra has to be considered because the vibrational relaxation and thus the changes of the probe sensitivity, are not identical for both excitations. Prepared in the $^1\Pi_1$ state, the wave packet has higher kinetic energy at $t = 0$ and thus the sensitivity is reduced. The energy loss increases with kinetic energy and the sensitivity rises quickly to the final value. The vibrational relaxation and sensitivity for times $t > 2$ ps are very similar in both cases according to the same shape of the envelopes. The correction will enlarge the signal (solid line) near $t = 0$ and thus bring the experimental values even closer to the theoretical data (Fig. 7.21b). To estimate the correction, the kinetic energy of the wave packet at the probe window is calculated for the first excursion. It is $E_{kin} = 6000$ cm^{-1} and 15800 cm^{-1} for B state and $^1\Pi$ excitation, respectively. Taking the sensitivity S as inversely proportional to the velocity [45] $S \sim 1/v \sim 1/\sqrt{E_{kin}}$ yields the correction factor $c = S_{triplet}/S_{\sin glet} = 1.6$ before the first collision with the matrix. At later times the correction is very close to 1.

The excitation to $B(^3\Pi_0)$ is a parallel transition [138, 140] ($\Delta\Omega = 0$), whereas to $^1\Pi_1$ it is perpendicular ($\Delta\Omega = 1$). The pump beams are chosen to have polarization parallel and perpendicular to the probe polarization, respectively, to avoid differences due to depolarization. The intensity ratio

[8] In Fig. 7.18 this is the thick solid line.

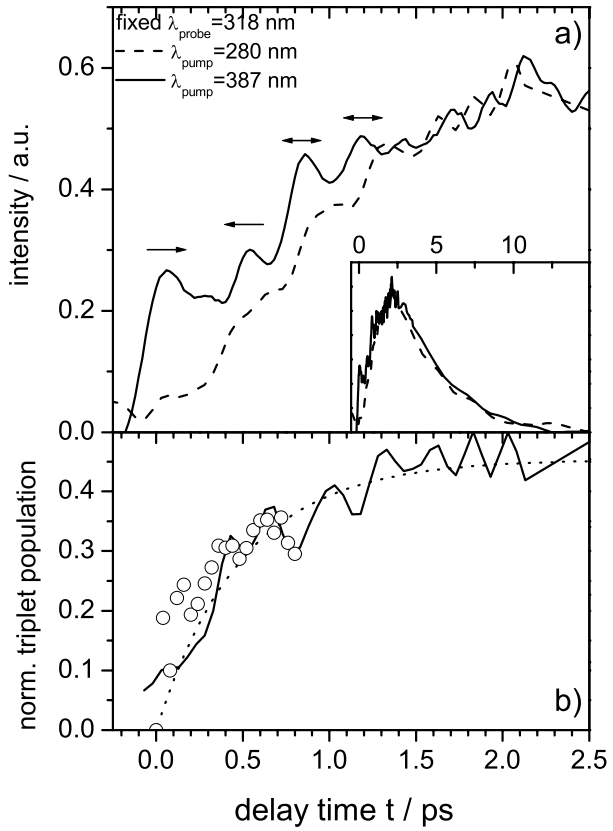

Figure 7.21: a) Pump-probe spectra with $\lambda_{probe} = 317$ nm, probing only the bound $^3\Pi$ states. The solid curve corresponds to excitation into the $B(^3\Pi_0)$ state with $\lambda_{pump} = 387$ nm and the dashed curve to $^1\Pi_1$ with $\lambda_{pump} = 280$ nm from Fig. 6.11. Both spectra show oscillations due to wave packet dynamics. b) Ratio of the two spectra, displaying the spin-flip from $^1\Pi$ into $^3\Pi$ (solid line). The dashed line is an exponential fit to the solid line with time constant $\tau_{pump} = 500$ fs. The open circles are taken from the simulation in ref. [71]

for probing the torus prepared with a $\Delta\Omega = 1$ transition on the $^1\Pi$ state by a $\cos^2\theta$ lobe ($\Delta\Omega = 0$) is 1/5 for parallel $(\|)$ and 2/5 for perpendicular $(\perp)$ pump probe polarization according to the last two lines of table 2.3.5. When probing the $\Delta\Omega = 0$ transition to the B state with another $\Delta\Omega = 0$ transition, the intensities are 3/5 for parallel $(\|)$ and 1/5 for perpendicular $(\perp)$ pump probe polarization. In order to achieve the same depolarization behavior for B and $^1\Pi$ state the equal ratios of 1/5 must be chosen. Otherwise the time dependence in the spectra from Fig. 7.21a would be different due to the depolarization, since the final value in both cases (after 2 ps) is given by $I_d = 1/3$ for a depolarized ensemble. The results on time dependent depolarization of ClF in Ar are discussed separately in chapter 2.3.5.

7.6.3 Comparison of experiment and theory

This experiment on ClF in solid Ar can be regarded as a test of the predictions of multidimensional semiclassical quantum theory for non-adiabatic transitions. Theory and experiment agree on important aspects in the sense that the experimental data are reproduced by the evolution of a large fraction of the simulated trajectories. Fig. 7.21b shows a nearly quantitative agreement of the timescale for accumulation of population in the bound triplet states for ClF in Ar (experiment: solid line) and F_2 in Ar (theory: open circles). After excitation of the molecule above its gas phase dissociation limit, the Ar surrounding forces ultrafast recombination onto the lowest set of electronically excited states. When the bond is stretched to the region ($R > 4.5\ a_0$) where the splitting of the states is very small (Fig. 7.20), the wave packet can undergo non-adiabatic transitions (surface hopping) to coupled states. Those which are kept on the repulsive states like $^1\Pi_1$ stay above the crossing region will always have the chance to decay non-adiabatically to the lower $^3\Pi$ states when the wave packet is in the interaction region (cf. Fig. 7.20 and Fig. 7.19). Thus substantial population of 40% is

accumulated in the bound triplet states within 1 ps and an exponential rise time of $\tau_f = 500$ fs (cf. Fig. 7.21b). τ_f measures the time it takes to dissociate ClF, flip the spin and recombine the molecule. The transition to the triplet state observed in the experiment (solid line) are especially strong between 250 and 400 fs, when the $Cl - F$ bond is stretched and all electronic states are nearly degenerate. The Ar cage confines the Cl and F within the region of high transition probability and at the same time dissipates a large fraction of the excess energy. In this way it directs the non-adiabatic transitions towards electronic states with lower energy. The excellent agreement allows the conclusion that the nonadiabatic molecular dynamics simulations capture the important processes.

The simulations on F_2/Ar derive a spin-flip time of approx. 60 fs (Fig. 7.18). It is the spin-orbit coupling that allows non-adiabatic transitions between singlet and triplet states. The spin-flip processes are very efficient and occur surprisingly rapidly in view of the weakness of the spin-orbit coupling. The F_2 molecule is lighter than ClF and is excited with higher excess energy in the simulations (the dissociation limit of F_2 is lower) and thus the dissociation is faster. After 60 fs the $F - F$ bond is stretched and thus the spin-flip occurs preferentially at large bond distances, in accordance with the experimental finding. All trajectories presented in ref. [71] show large surface hopping probability among the coupled states for bond distances $R > 4.5$ a_0. This coincides with the observation that the electronic states are very close to each other in this region (Fig. 7.20).

In the interpretation of the trajectory simulations previously given [71, 221, 222], it was stated that the ratio between the population of the singlet and triplet states reaches the statistical equilibrium (1 : 3) in the first excursion. The statistical distribution with larger weight on the triplets can explain why recombination on the excited triplet state is preferred to recombination onto the ground state. It will be instructive to disentangle the effects that electrostatic interactions and spin-orbit coupling in the fragments have on the recombining molecular orbital occupation.

The measured rise time of the triplet population ($\tau_f = 500$ fs) in ClF agrees nearly quantitatively with the calculated population rise in F_2 (cf. Fig. 7.21b). In the future, the recombination onto the ground state should be measured as well as the decreasing population in the initially excited singlet state to complement the information on the triplet states. In this way it can be checked, whether the predicted statistical population of singlet vs. triplet states is established very fast within 60 fs, while the bond is stretched, and the relation to the 500 fs feeding time of the triplet states can be clarified. The singlet ion-pair manifold lies very high in energy and probe wavelengths $\lambda_{probe} \sim 240$ nm are required. The potential surfaces for the gas phase predict the minimum of the difference potential at $R_{win} = 4.6$ a_0 and $E_{win} = 21200$ cm^{-1}. The outward motion of the wave packet must be observable and the returning wave packet should have sufficient energy to reach the window a second time.

In principle the repulsive triplets can be probed with wavelengths longer than $\lambda_{probe} = 322$ nm, however the transition dipoles decrease at large $Cl - F$ distances [121]. At small internuclear separations the repulsion of these triplet states requires very high energy of the returning wave packet (cf. Fig. 5.6). The strong energy loss in the first encounter probably explains why this transition was never observed, although it was attempted to record pump-probe spectra with $\lambda_{probe} < 322$ nm.

7.6.4 Comparison to I_2 and Cl_2

In the corresponding spectra for Cl_2/Ar (Fig. 6.17) and I_2/Kr (Fig. 6.6), a very similar behavior is observed. These spectra are recorded for probing deeper in the bound state. Therefore the signal intensity in the first ps is weak and the normalization made for ClF, $I_{\mathrm{sin}\,glet}/I_{triplet}$, is noisy. It is evident that for $t > 1$ ps the spectra for singlet and triplet excitation agree nearly perfectly. Although in the heavier I_2 molecule the intersystem crossing is not surprising, the similarity of the spectra emphasizes the fact, that energy dissipation becomes highly nonlinear in the strong coupling limit. The singlet excitation in the case of I_2/Kr at $\lambda_{pump} = 480$ nm provides the I fragments with an energy of $E_{pump} = 9300$ cm^{-1}. Direct excitation to the triplet $^3\Pi_1$ at $\lambda_{pump} = 670$ nm results in

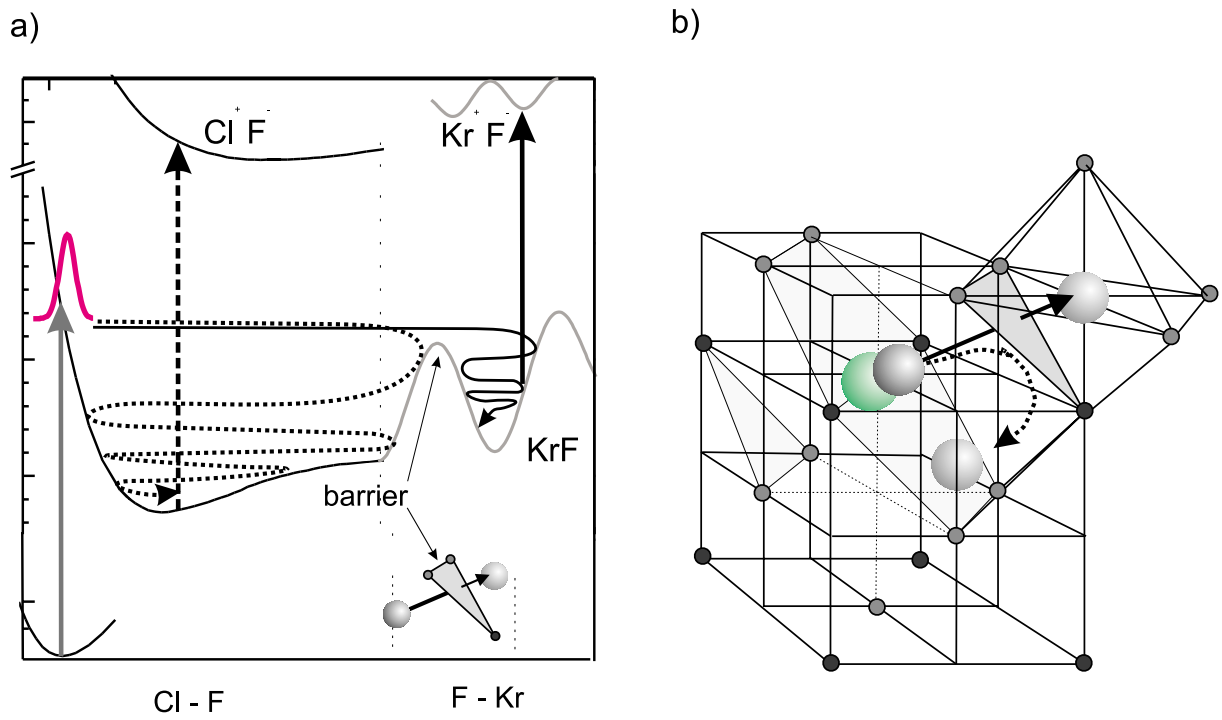

Figure 7.22: a) Potential energy surface of ClF/Kr. The pump pulse excites a $Cl-F$ wave packet, which can either undergo recombination (dashed arrow) in the original cage, or leave the cage by overcoming the barrier (solid arrow). After cage exit the F fragment can be probed by excitation to the Kr^+F^- state. b) Dissociation (solid arrow) vs. recombination (dashed arrow) of ClF in the three dimensional Kr latttice.

$E_{pump} = 3390$ cm^{-1}. Nonetheless both spectra agree for $t > 1$ ps. Obviously the three times higher excess energy prepared in the singlet state is dissipated just as well by the Kr matrix.

7.7 Cage exit dynamics of ClF in Kr

Until this chapter, femtosecond pump-probe spectra of ClF/Ar were analyzed with probe windows in the molecular $Cl-F$ coordinate, which are sensitive to the rich recombination dynamics. This is indicated in Fig. 7.22 by the dashed arrows. From the static experiments on photodissociation of ClF in Kr, it is evident that a large fraction of molecules is permanently dissociated (chapter 5.4.1). The F fragments can be probed via the Kr^+F^- excimer (chapter 4.2.4), i.e. in the $Kr-F$ coordinate. Fig. 7.22a sketches the potential energy surface, and the solid arrows display the cage exit dynamics. For a dissociation of ClF with cage exit of the F fragment, the wave packet prepared by the pump pulse has to overcome the barrier imposed by the gray shaded triangle of Kr atoms. Behind the barrier, the F fragment is surrounded by Kr atoms, and it can be detected by a probe pulse to the Kr^+F^- states. Fig. 7.22b displays the competition of recombination and the cage exit in the three dimensional Kr lattice.

7.7.1 Direct versus delayed exit

The simulations [67, 71] show two ways in which the dissociation of F_2 in Ar can proceed on the fs timescale, and this behavior is more generally observed for photodynamics of molecules in solid rare gases [36]. A direct dissociation proceeds with cage exit after 250 fs, and in the delayed dissociation events the F fragments leave the cage after one or two collisions with the surrounding, e.g. after 1 ps. Trajectories displaying these dynamics from ref. [71] are reproduced in Fig. 7.23.

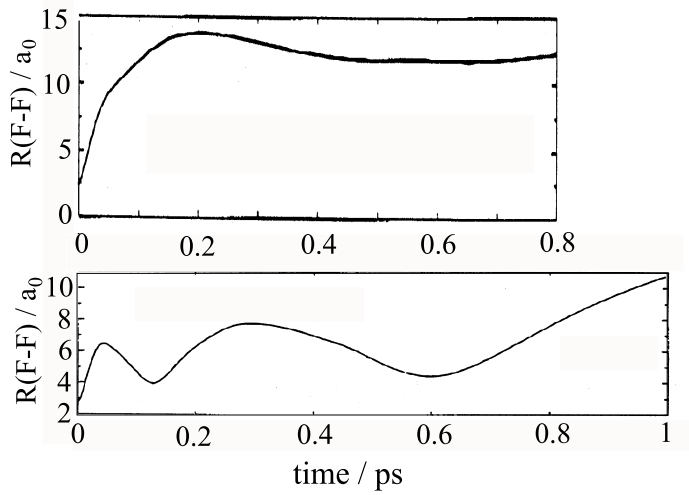

Figure 7.23: Trajectories $R(t)$ taken from the DIM simulations on F_2/Ar in ref. [71]. Panel a) shows a trajectory with direct cage exit after 200 fs. Panel b) demonstrates the delayed cage exit after 1ps. In this trajectory two collisions with the cage walls (at 100 and 300 fs) occur before dissociation.

Figs. 6.12 and 6.13 show pump-probe spectra for ClF/Kr with $\lambda_{pump} = 387$ nm. The ClF dissociation provides the F fragment with a kinetic energy of $E_{kin} = 3070$ cm^{-1}. All spectra have a peak around 300 fs, which is predicted for the direct cage exit. In the spectrum for $\lambda_{probe} = 270$ nm at $T = 4$ K (Fig. 6.13a), for example, the interpretation is straight forward. 270 nm probe F atoms in the center of the O_h site after they escaped from the original substitutional site of the ClF molecule. If the peak at negative time delay (discussed below) is subtracted, the signal is zero at the time origin and rises after 150 fs to reach the first maximum at 300 fs, when the F atoms have reached the center of the O_h site. This corresponds to a straight flight of the F fragment from the initial substitutional site to the O_h site through the Ar_3 triangle, as indicated in Fig. 7.22b. In an estimate that assumes free motion of F with a kinetic energy of $E_{kin} = 3000$ cm^{-1}, it takes 250 fs to travel the distance of 0.49 nm. This time imposes a lower limit, since the fragment will lose some of its energy and move more slowly. In the calculated trajectory for F_2/Ar displayed in Fig. 7.23a, the cage exit is faster than 200 fs, because the molecule is prepared with more than twice the kinetic energy.

The subsequent dynamics cannot be unambiguously assigned at the moment. The peaks at 600 fs and 1 ps may originate either from delayed cage exit (Fig. 7.23b) or from further migration of the F atoms to more remote sites. However, the broad feature at 1 ps that is clearly seen for probing with $\lambda_{probe} = 270$ nm at $T = 20$ K (Fig. 6.13c) most likely corresponds to the delayed cage exit. The time for delayed exit is not as well defined as for the direct cage exit and the broad peak at 1 ps corresponds to the broad distribution of different scattering parameters. Statistics on the trajectories displaying delayed cage exit like Fig. 7.23b are missing but are in preparation in the collaborating theory groups. Fig. 7.10b shows the 2-D quantum simulation for F_2/Ar with pre-excitation of the Ar_3 mode to the 6^{th} vibrational level. While the cage exit without pre-excitation is zero within the simulated 1 ps, a high probability for delayed cage exit is observed after 0.7 ps, where the Ar_3 triangle is pre-excited. This corroborates the assignment of the broad peak around 1 ps to the delayed cage exit, which occurs preferentially in warm samples (20 K), with an excited lattice.

7.7.2 Two ultrafast pathways to $Kr_2^+F^-$

It was mentioned in chapter 6.3.4 that the peak at $t = -50$ fs depends quadratically on the intensity I_{387} of the pulse at 387 nm. This suggests an explanation of this feature in terms of process b) sketched in Fig. 7.24. A pump pulse at 270 nm excites ClF to its $^1\Pi$ state. A two photon resonance with 387 nm leads high into the ion-pair manifold of Cl^+F^-. A wave packet is prepared in the ionic states which corresponds to an F^- ion with sufficient energy to overcome the barrier to the next Kr cage within the ionic manifold. The F^- ion exits the solvent cage and subsequent structural rearrangement leads to formation of the $Kr_2^+F^-$ exciplex. This process occurs for the inverted pulse sequence with

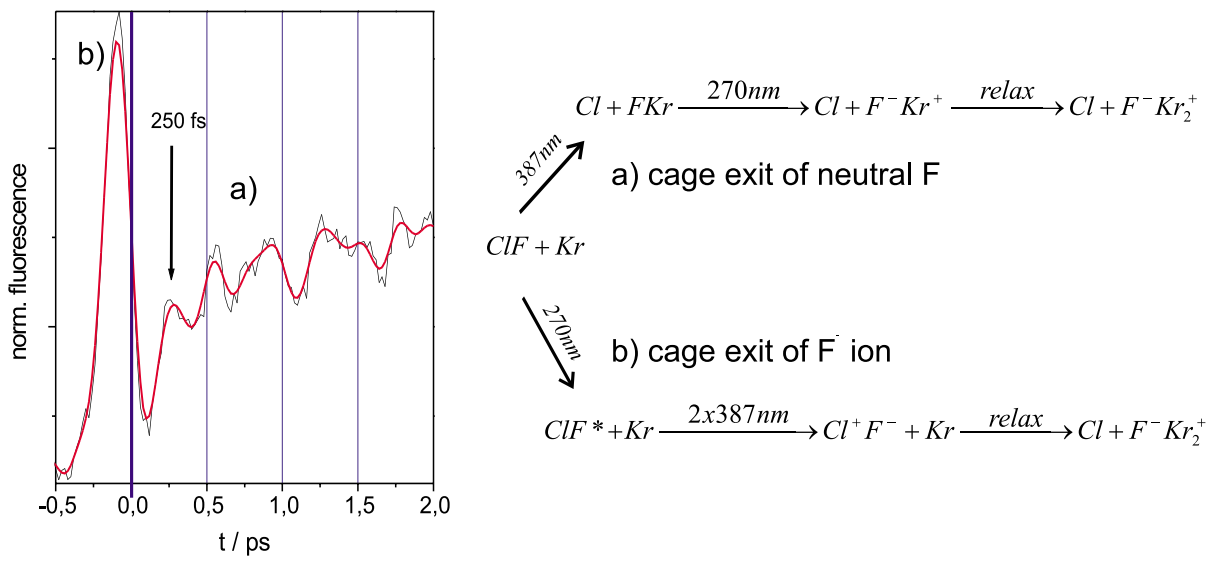

Figure 7.24: Pump-probe spectrum demonstrating cage exit of F in Kr. For positive time delays, the cage exit proceeds via the neural F fragment (process a). The arrival time of the F fragment in the nearest site is 250 fs. For negative time delays the cage exit of the F^- ion is observed (process b).

negative time delay. The peak at $t = -50$ fs suggests that the two photon resonance occurs on the repulsive inner limb of the ClF potential This is supported by the difference potential for the singlet states (Fig. 2.11).

For positive time delay, the pump-pulse $\lambda_{pump} = 387$ nm dissociates ClF and the neutral F fragment leaves the cage as described in chapter 7.7.1. After ~ 250 fs, the F fragment has reached the nearest O_h site and the 270 nm pulse excites the excimer Kr^+F^-. Again structural rearrangement leads to the formation of the fluorescing $Kr_2^+F^-$ exciplex.

7.7.3 Vibration of the Kr cage around F fragments

The pump-probe spectrum in Fig. 6.14 is surprisingly well modulated and the oscillational period increases from 550 fs to 750 fs in the first 4 periods. The assignment of the fluorescence to the $Kr_2^+F^-$ exciplex suggests that this oscillation corresponds to a vibrational mode of the Kr cage around an F fragment. In an anharmonic Morse like molecular potential, the vibrational relaxation would lead to a decreasing period of the vibration, when the harmonic part of the potential is approached (cf. chapter 7.4.2). This is contrary to the observation. On the other hand, the steep van-der-Waals potentials, that govern the $Kr - Kr$ interaction, give rise to potentials with a broad flat minimum and steep walls, that resemble the a square well. In these potentials, higher excitation results in higher frequencies and this would explain the observed slowing down of the vibration in Fig. 6.14 in the course of vibrational relaxation. Moreover, periods around 650 fs are typical for modes of the Kr lattice and are also observed in spectra of I_2/Kr after the dominant I_2 oscillation has decayed [29]. These solvent modes show up in the pump-probe spectra, when the probe wavelength is reduced below the excitation threshold for the resonance of the molecule isolated in the static lattice (e.g. spectra with $\lambda_{probe} = 540$ nm in the Appendix). As was detailed at the end of chapter 7.3.2, the solvent breathing shifts the strongly solvated ionic potentials and thus leads to modulation of the observed spectra.

A microscopic view of the process is suggested from the geometry of the cage exit shown in Fig. 7.22. The F atom points at a triangle of Kr atoms. After photodissociation of ClF, the F atom kicks this triangular window and traverses it. The interaction time of F with the three Kr atoms is well

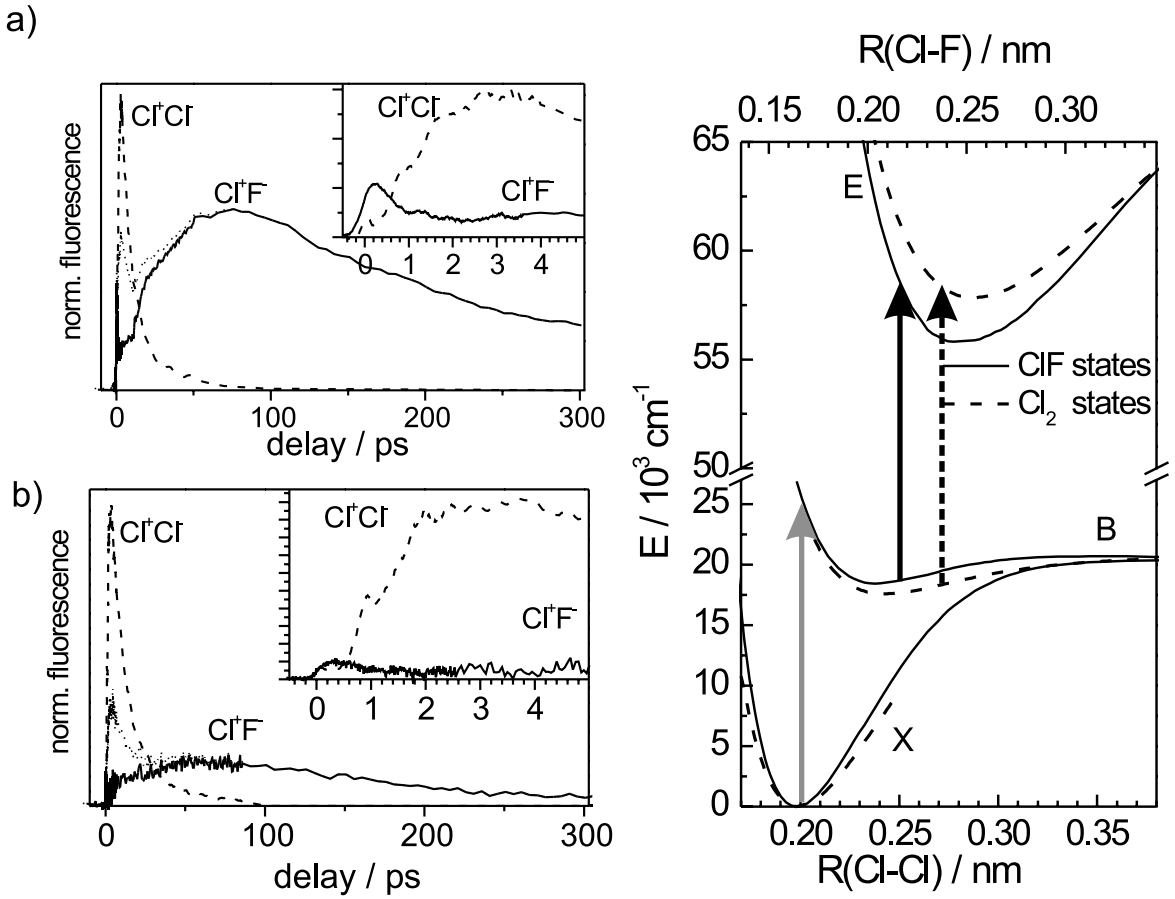

Figure 7.25: Control of Cl^+Cl^- vs. Cl^+F^- population demonstrated by pump-probe spectra on $Cl_2 : ClF : Ar$ samples at the concentration $1 : 100 : 100,000$. Both species are excited with $\lambda_{pump} = 387$ nm. The fluorescence $\lambda_{LIF} = 420$ nm monitors Cl_2 and ClF (dotted), $\lambda_{LIF} = 360$ nm monitors Cl_2 only (dashed). From these traces the ClF signal is calculated (solid). a) $\lambda_{probe} = \lambda_{control} = 282$ nm, b) $\lambda_{probe} = \lambda_{control} = 282$ nm. c) Unshifted potential surfaces for ClF and Cl_2. The bond distance of ClF (top scale) is calibrated to obtain the same equilibrium position as for Cl_2 (bottom scale). The potentials are very similar. The dashed and the solid arrow indicate the probe window for Cl_2 and ClF, respectively.

defined and this will trigger coherent motion of the Kr atoms. The F is now in the interstitial O_h site (Fig. 7.22b) and vibrationally relaxes. The coherent modulation of the Kr cage size shifts the ionic Kr^+F^- states, formed by the F fragment with either of the Kr cage atoms, up and down and this produces the observed oscillations. The rise and decay of the signal envelope shown in the inset is a signature of vibrational relaxation of the F atom within the cage and energy loss from the Kr mode.

This interpretation should be confirmed in the future by MD simulations on ClF/Kr. Trajectory calculations can be found on the related system NO in Ar [215]. NO is isolated on a substitutional site of an Ar lattice. Excitation to a Rydberg state of NO leads to an impulsive cage breathing. The simulations corroborate the slowing down of the cage vibration.

7.8 Relaxation-time-control of Cl_2 vs. ClF

Recent experiments aim at an extension of coherent control or quantum control strategies to molecules in condensed phases, i.e. to systems with dissipation. In the Gerber group evolutionary strategies

are used to find the optimal pulse sequence to steer the fluorescence of two substances with nearly identical absorptions in the liquid phase [223] and a contrast ratio of $1:1.5$ is obtained. Based on the fact that shaped laser pulses can control the relative fluorescence from the two molecules, the authors conclude that coherences must survive at least for the timescale of 100 fs.

This chapter treats the experiments on a solid Ar sample, doped with $Cl_2 : ClF : Ar$ at a relative concentration of $1 : 1000 : 100,000$, in the spirit of control with ultrafast laser pulses in a double pulse scenario (Tannor-Kosloff-Rice scheme [15, 16, 20]). $\lambda_{pump} = 387$ nm excites Cl_2 and ClF with nearly equal probability as can be judged from the $A' \rightarrow X$ fluorescence intensities (Fig. 4.2)[9]. The wavelengths $\lambda_{probe} = 280$ and 282 nm probe Cl_2 and ClF to their ionic states Cl^+Cl^- and Cl^+F^- (Fig. 7.25a and b). The fluorescence intensity from these ion-pair states is proportional to the number of these ion-pair species produced in the double pulse sequence. Now, the control target is to maximize the yield of one of the two ion-pair species, i.e. its fluorescence. The only parameter varied in this control scheme is the time delay between $\lambda_{pump} = 387$ nm and $\lambda_{control} = 280$ or 282 nm.

When the fluorescence is detected at $\lambda_{LIF} = 420$ nm (dotted line in Fig. 7.25a), both molecules contribute to the signal (cf. Fig. 4.8a and b). Fluorescence at $\lambda_{LIF} = 360$ nm is exclusively due to Cl_2 (cf. Fig. 4.8). The pump-probe spectrum for $\lambda_{control} = 282$ nm with $\lambda_{LIF} = 360$ nm is indicated by a dashed line in Fig. 7.25a. The dashed spectrum is used to decompose the dotted spectrum ($\lambda_{LIF} = 420$ nm) into a signal for Cl_2 and ClF. The resulting ClF contribution is shown in Fig. 7.25a as a solid line.

The inset in Fig. 7.25a shows the decomposed fluorescence intensities I_{ClF} (solid) and I_{Cl_2} (dashed), and therefore the number of excited ion-pair species Cl^+F^- vs. Cl^+Cl^- on a shorter timescale. In the maximum of the Cl^+Cl^- signal at time $t = 3$ ps, the ratio of the excited molecules is $I_{ClF}/I_{Cl_2} = 1/5$. For times $t > 70$ ps I_{Cl_2} almost vanishes and I_{ClF} has a maximum at $t = 70$ ps. The contrast ratio at this time is better than $I_{ClF}/I_{Cl_2} = 50/1$. Thus by varying the time delay from 3 ps to 70 ps the ratio between ClF and Cl_2 fluorescence can be switched by a factor 250 in this one parameter control scheme. In view of the similarity of the two PES for Cl_2 and ClF (Fig. 5.7) the contrast ratios obtained are excellent. For a $Cl_2 : ClF$ concentration of $1:1$, the contrast at $t = 3$ ps in favor of Cl_2 would improve to $500:1$.

Fig. 7.25b shows the same procedure for a different control wavelength $\lambda_{control} = 280$ nm and an even better switching between ClF and Cl_2 ion-pair species is obtained. Again ClF dominates for $t > 100$ ps, while the Cl_2 fluorescence is zero. At $t = 3$ ps on the other hand, $I_{ClF}/I_{Cl_2} = 1/10$.

Besides the control on the ps timescale, control on the femtosecond timescale can be seen in Fig. 7.25a in the early peak at 50 fs, which belongs to Cl^+F^- (solid line), whereas from 1 ps onwards the Cl^+Cl^- signal (dashed) dominates. In chapter 7.3.2 the early peak is identified as the outward moving ClF wave packet. This demonstrates the selective excitation of Cl_2 vs. ClF on the femtosecond timescale as wave packet timing control with a contrast ratio of $1:3.4$. For an optimized control wavelength this can be improved.

The maxima in Fig. 7.25a at $t = 3$ ps for Cl^+Cl^- and at $t = 100$ ps for Cl^+F^- are due to vibrational relaxation (cf. chapter 7.4). Therefore the term relaxation-time control may be adequate. Fig. 7.25c reproduces the potential surfaces of ClF and Cl_2 and shows the probe window for ClF by the solid arrow and for Cl_2 by the dotted arrow. The relaxation-time control scheme delivers excellent contrast ratios. The population in high vibrational levels of Cl_2 quickly decays below the probe window and the resonance to Cl^+Cl^- is lost. Obviously, this control scheme is entirely incoherent, as it makes use of vibrationally relaxed population in the intermediate state. The wave packet timing control around 50 fs exploits the wave packet motion in a Tannor-Kosloff-Rice scheme [15, 16, 20]. However, a quantum mechanical coherence is not necessary in this scheme either.

[9] The much larger absorption of Cl_2 compared to ClF balances the lower concentration.

7.9 Dissipation and vibrational coherence

In chapter 7.3, the spectra for I_2/Kr and ClF/Ar were analyzed in terms of wave packet dynamics. The wave packet is initially prepared in the molecular $I-I$ or $Cl-F$ coordinate. In the first oscillation of the molecule, a substantial fraction of the energy is already transferred to the solvent by collisions of the molecular fragments with the cage. Despite the dramatic energy loss, the pump-probe transients show oscillations due to vibrational coherence. Moreover, the collision induces vibrational motion of the cage atoms. This in turn appears in the pump-probe spectra, since changing the size of the solvent cavity shifts the strongly solvated ion-pair states of the molecule up and down with the coherent oscillations of the cage breathing [29]. If a probe wavelength close to the threshold is chosen, the probe transition is shifted into and out of resonance periodically..

Energy dissipation is intimately connected to decoherence, since the interaction of the originally excited molecule with the "bath" of atoms induces both processes. The results of this thesis demonstrate that a strong dissipation of energy can take place in a way that preserves the vibrational coherence of the wave packet to a large extent. Even after the strongest collisions at high energy (e.g. Fig. 6.2), the oscillations survive for several ps. Inspection of the spectra on a longer timescale (Fig. 6.4a) reveals that the contributions from an unmodulated background increase with the interaction energy, since the modulations decay faster for shorter pump wavelength. This background is a signature of the decoherence of the wave packet, which is induced by the random distribution of scattering conditions. However, the detection of the coherence with the probe pulse must be considered, as well. The spectra in Fig. 6.2b and 6.4b, that probe a wave packet excited at the dissociation limit of I_2 at $\lambda_{pump} = 500$ nm with different λ_{probe}, demonstrate that the background increases with shorter $\lambda_{probe,}$ as the probe window moves to lower energies E_{win}. The background disappears entirely if the wave packet is probed with a window below resonance ($\lambda_{probe} = 530$ and 540 nm). The reason for this is closely related to the effect of the probe window on the apparent vibrational period discussed in chapter 7.2. If the probe window energy E_{win} is above the energy of the wave packet, then only the highest fraction of vibrational levels that make up the wave packet are recorded. The population in these levels has not yet suffered the energy loss and the decoherence is negligible. A probe window in the potential minimum, on the other hand, monitors all parts of the wave packet. The energy of the wave packet determines the detection sensitivity, which scales with the velocity as $1/v$ or with the energy E of the vibrational level as $1/\sqrt{E}$. Thus the wave packet is probed over a broad range of energies and thus different scattering parameters with comparable sensitivity. This blurs the modulations in the spectra. The trend, that the modulation depth decreases with shorter probe wavelength is observed as well in ClF/Ar.

The theoretical description of wave packets that experience dissipation still in its infancy. The loss of coherence has to be implemented in the density matrix formalism by empirical parameters. In reduced dimensionality approaches the problem is manifest in the somewhat arbitrary definition of the quantum mechanical "system" and the "bath". The detailed experimental results in the model systems presented here will allow testing further predictions from theory.

The preserved vibrational coherence observed even in the regime of strong system-bath coupling demonstrates that there is good prospect to coherent control in condensed phase reactions.